Measurement of differential production cross section for Z/γ^* bosons in association with jets in $p\bar{p}$ collisions at $\sqrt{s} = 1.96$ TeV

Aaltonen, T A ; Amerio, S ; Amidei, D E ; et al ; Canelli, F ; Kilminster, B ; CDF Collaboration

Abstract: Differential cross sections for the production of Z bosons or off-shell photons γ^* in association with jets are measured in proton-antiproton collisions at center-of-mass energy $\sqrt{s} = 1.96$ TeV using the full data set collected with the Collider Detector at Fermilab in Tevatron Run II, and corresponding to 9.6 fb^{-1} of integrated luminosity. Results include first measurements at CDF of differential cross sections in events with a Z/γ^* boson and three or more jets, the inclusive cross section for production of Z/γ^* and four or more jets, and cross sections as functions of various angular observables in lower jet-multiplicity final states. Measured cross sections are compared to several theoretical predictions.

DOI: https://doi.org/10.1103/PhysRevD.91.012002

Measurement of differential production cross section for Z/γ^* bosons in association with jets in $p\bar{p}$ collisions at $\sqrt{s} = 1.96$ TeV

T. Aaltonen,[21] S. Amerio[jj],[39] D. Amidei,[31] A. Anastassov[v],[15] A. Annovi,[17] J. Antos,[12] G. Apollinari,[15] J.A. Appel,[15] T. Arisawa,[52] A. Artikov,[13] J. Asaadi,[47] W. Ashmanskas,[15] B. Auerbach,[2] A. Aurisano,[47] F. Azfar,[38] W. Badgett,[15] T. Bae,[25] A. Barbaro-Galtieri,[26] V.E. Barnes,[43] B.A. Barnett,[23] P. Barria[ll],[41] P. Bartos,[12] M. Bauce[jj],[39] F. Bedeschi,[41] S. Behari,[15] G. Bellettini[kk],[41] J. Bellinger,[54] D. Benjamin,[14] A. Beretvas,[15] A. Bhatti,[45] K.R. Bland,[5] B. Blumenfeld,[23] A. Bocci,[14] A. Bodek,[44] D. Bortoletto,[43] J. Boudreau,[42] A. Boveia,[11] L. Brigliadori[ii],[6] C. Bromberg,[32] E. Brucken,[21] J. Budagov,[13] H.S. Budd,[44] K. Burkett,[15] G. Busetto[jj],[39] P. Bussey,[19] P. Butti[kk],[41] A. Buzatu,[19] A. Calamba,[10] S. Camarda,[4] M. Campanelli,[28] F. Canelli[cc],[11] B. Carls,[22] D. Carlsmith,[54] R. Carosi,[41] S. Carrillo[l],[16] B. Casal[j],[9] M. Casarsa,[48] A. Castro[ii],[6] P. Catastini,[20] D. Cauz[qqrr],[48] V. Cavaliere,[22] A. Cerri[e],[26] L. Cerrito[q],[28] Y.C. Chen,[1] M. Chertok,[7] G. Chiarelli,[41] G. Chlachidze,[15] K. Cho,[25] D. Chokheli,[13] A. Clark,[18] C. Clarke,[53] M.E. Convery,[15] J. Conway,[7] M. Corbo[y],[15] M. Cordelli,[17] C.A. Cox,[7] D.J. Cox,[7] M. Cremonesi,[41] D. Cruz,[47] J. Cuevas[x],[9] R. Culbertson,[15] N. d'Ascenzo[u],[15] M. Datta[ff],[15] P. de Barbaro,[44] L. Demortier,[45] M. Deninno,[6] M. D'Errico[jj],[39] F. Devoto,[21] A. Di Canto[kk],[41] B. Di Ruzza[p],[15] J.R. Dittmann,[5] S. Donati[kk],[41] M. D'Onofrio,[27] M. Dorigo[ss],[48] A. Driutti[qqrr],[48] K. Ebina,[52] R. Edgar,[31] A. Elagin,[47] R. Erbacher,[7] S. Errede,[22] B. Esham,[22] S. Farrington,[38] J.P. Fernández Ramos,[29] R. Field,[16] G. Flanagan[s],[15] R. Forrest,[7] M. Franklin,[20] J.C. Freeman,[15] H. Frisch,[11] Y. Funakoshi,[52] C. Galloni[kk],[41] A.F. Garfinkel,[43] P. Garosi[ll],[41] H. Gerberich,[22] E. Gerchtein,[15] S. Giagu,[46] V. Giakoumopoulou,[3] K. Gibson,[42] C.M. Ginsburg,[15] N. Giokaris,[3] P. Giromini,[17] V. Glagolev,[13] D. Glenzinski,[15] M. Gold,[34] D. Goldin,[47] A. Golossanov,[15] G. Gomez,[9] G. Gomez-Ceballos,[30] M. Goncharov,[30] O. González López,[29] I. Gorelov,[34] A.T. Goshaw,[14] K. Goulianos,[45] E. Gramellini,[6] C. Grosso-Pilcher,[11] R.C. Group,[51,15] J. Guimaraes da Costa,[20] S.R. Hahn,[15] J.Y. Han,[44] F. Happacher,[17] K. Hara,[49] M. Hare,[50] R.F. Harr,[53] T. Harrington-Taber[m],[15] K. Hatakeyama,[5] C. Hays,[38] J. Heinrich,[40] M. Herndon,[54] A. Hocker,[15] Z. Hong,[47] W. Hopkins[f],[15] S. Hou,[1] R.E. Hughes,[35] U. Husemann,[55] M. Hussein[aa],[32] J. Huston,[32] G. Introzzi[nnoo],[41] M. Iori[pp],[46] A. Ivanov[o],[7] E. James,[15] D. Jang,[10] B. Jayatilaka,[15] E.J. Jeon,[25] S. Jindariani,[15] M. Jones,[43] K.K. Joo,[25] S.Y. Jun,[10] T.R. Junk,[15] M. Kambeitz,[24] T. Kamon,[25,47] P.E. Karchin,[53] A. Kasmi,[5] Y. Kato[n],[37] W. Ketchum[gg],[11] J. Keung,[40] B. Kilminster[cc],[15] D.H. Kim,[25] H.S. Kim,[25] J.E. Kim,[25] M.J. Kim,[17] S.H. Kim,[49] S.B. Kim,[25] Y.J. Kim,[25] Y.K. Kim,[11] N. Kimura,[52] M. Kirby,[15] K. Knoepfel,[15] K. Kondo,[52,*] D.J. Kong,[25] J. Konigsberg,[16] A.V. Kotwal,[14] M. Kreps,[24] J. Kroll,[40] M. Kruse,[14] T. Kuhr,[24] M. Kurata,[49] A.T. Laasanen,[43] S. Lammel,[15] M. Lancaster,[28] K. Lannon[w],[35] G. Latino[ll],[41] H.S. Lee,[25] J.S. Lee,[25] S. Leo,[41] S. Leone,[41] J.D. Lewis,[15] A. Limosani[r],[14] E. Lipeles,[40] A. Lister[a],[18] H. Liu,[51] Q. Liu,[43] T. Liu,[15] S. Lockwitz,[55] A. Loginov,[55] D. Lucchesi[jj],[39] A. Lucà,[17] J. Lueck,[24] P. Lujan,[26] P. Lukens,[15] G. Lungu,[45] J. Lys,[26] R. Lysak[d],[12] R. Madrak,[15] P. Maestro[ll],[41] S. Malik,[45] G. Manca[b],[27] A. Manousakis-Katsikakis,[3] L. Marchese[hh],[6] F. Margaroli,[46] P. Marino[mm],[41] K. Matera,[22] M.E. Mattson,[53] A. Mazzacane,[15] P. Mazzanti,[6] R. McNulty[i],[27] A. Mehta,[27] P. Mehtala,[21] C. Mesropian,[45] T. Miao,[15] D. Mietlicki,[31] A. Mitra,[1] H. Miyake,[49] S. Moed,[15] N. Moggi,[6] C.S. Moon[y],[15] R. Moore[ddee],[15] M.J. Morello[mm],[41] A. Mukherjee,[15] Th. Muller,[24] P. Murat,[15] M. Mussini[ii],[6] J. Nachtman[m],[15] Y. Nagai,[49] J. Naganoma,[52] I. Nakano,[36] A. Napier,[50] J. Nett,[47] C. Neu,[51] T. Nigmanov,[42] L. Nodulman,[2] S.Y. Noh,[25] O. Norniella,[22] L. Oakes,[38] S.H. Oh,[14] Y.D. Oh,[25] I. Oksuzian,[51] T. Okusawa,[37] R. Orava,[21] L. Ortolan,[4] C. Pagliarone,[48] E. Palencia[e],[9] P. Palni,[34] V. Papadimitriou,[15] W. Parker,[54] G. Pauletta[qqrr],[48] M. Paulini,[10] C. Paus,[30] T.J. Phillips,[14] E. Pianori,[40] J. Pilot,[7] K. Pitts,[22] C. Plager,[8] L. Pondrom,[54] S. Poprocki[f],[15] K. Potamianos,[26] A. Pranko,[26] F. Prokoshin[z],[13] F. Ptohos[g],[17] G. Punzi[kk],[41] I. Redondo Fernández,[29] P. Renton,[38] M. Rescigno,[46] F. Rimondi,[6,*] L. Ristori,[41,15] A. Robson,[19] T. Rodriguez,[40] S. Rolli[h],[50] M. Ronzani[kk],[41] R. Roser,[15] J.L. Rosner,[11] F. Ruffini[ll],[41] A. Ruiz,[9] J. Russ,[10] V. Rusu,[15] W.K. Sakumoto,[44] Y. Sakurai,[52] L. Santi[qqrr],[48] K. Sato,[49] V. Saveliev[u],[15] A. Savoy-Navarro[y],[15] P. Schlabach,[15] E.E. Schmidt,[15] T. Schwarz,[31] L. Scodellaro,[9] F. Scuri,[41] S. Seidel,[34] Y. Seiya,[37] A. Semenov,[13] F. Sforza[kk],[41] S.Z. Shalhout,[7] T. Shears,[27] P.F. Shepard,[42] M. Shimojima[t],[49] M. Shochet,[11] I. Shreyber-Tecker,[33] A. Simonenko,[13] K. Sliwa,[50] J.R. Smith,[7] F.D. Snider,[15] H. Song,[42] V. Sorin,[4] R. St. Denis,[19,*] M. Stancari,[15] D. Stentz[v],[15] J. Strologas,[34] Y. Sudo,[49] A. Sukhanov,[15] I. Suslov,[13] K. Takemasa,[49] Y. Takeuchi,[49] J. Tang,[11] M. Tecchio,[31] P.K. Teng,[1] J. Thom[f],[15] E. Thomson,[40] V. Thukral,[47] D. Toback,[47] S. Tokar,[12] K. Tollefson,[32] T. Tomura,[49] D. Tonelli[e],[15] S. Torre,[17] D. Torretta,[15] P. Totaro,[39] M. Trovato[mm],[41] F. Ukegawa,[49] S. Uozumi,[25] F. Vázquez[l],[16] G. Velev,[15] C. Vellidis,[15] C. Vernieri[mm],[41] M. Vidal,[43] R. Vilar,[9] J. Vizán[bb],[9] M. Vogel,[34] G. Volpi,[17] P. Wagner,[40] R. Wallny[j],[15] S.M. Wang,[1] D. Waters,[28] W.C. Wester III,[15] D. Whiteson[c],[40] A.B. Wicklund,[2] S. Wilbur,[7] H.H. Williams,[40] J.S. Wilson,[31] P. Wilson,[15] B.L. Winer,[35] P. Wittich[f],[15] S. Wolbers,[15] H. Wolfe,[35] T. Wright,[31] X. Wu,[18] Z. Wu,[5] K. Yamamoto,[37] D. Yamato,[37] T. Yang,[15] U.K. Yang,[25] Y.C. Yang,[25] W.-M. Yao,[26] G.P. Yeh,[15] K. Yi[m],[15]

J. Yoh,[15] K. Yorita,[52] T. Yoshida[k],[37] G.B. Yu,[14] I. Yu,[25] A.M. Zanetti,[48] Y. Zeng,[14] C. Zhou,[14] and S. Zucchelli[ii6]
(CDF Collaboration)[†]

[1]*Institute of Physics, Academia Sinica, Taipei, Taiwan 11529, Republic of China*
[2]*Argonne National Laboratory, Argonne, Illinois 60439, USA*
[3]*University of Athens, 157 71 Athens, Greece*
[4]*Institut de Fisica d'Altes Energies, ICREA, Universitat Autonoma de Barcelona, E-08193, Bellaterra (Barcelona), Spain*
[5]*Baylor University, Waco, Texas 76798, USA*
[6]*Istituto Nazionale di Fisica Nucleare Bologna, [ii]University of Bologna, I-40127 Bologna, Italy*
[7]*University of California, Davis, Davis, California 95616, USA*
[8]*University of California, Los Angeles, Los Angeles, California 90024, USA*
[9]*Instituto de Fisica de Cantabria, CSIC-University of Cantabria, 39005 Santander, Spain*
[10]*Carnegie Mellon University, Pittsburgh, Pennsylvania 15213, USA*
[11]*Enrico Fermi Institute, University of Chicago, Chicago, Illinois 60637, USA*
[12]*Comenius University, 842 48 Bratislava, Slovakia; Institute of Experimental Physics, 040 01 Kosice, Slovakia*
[13]*Joint Institute for Nuclear Research, RU-141980 Dubna, Russia*
[14]*Duke University, Durham, North Carolina 27708, USA*
[15]*Fermi National Accelerator Laboratory, Batavia, Illinois 60510, USA*
[16]*University of Florida, Gainesville, Florida 32611, USA*
[17]*Laboratori Nazionali di Frascati, Istituto Nazionale di Fisica Nucleare, I-00044 Frascati, Italy*
[18]*University of Geneva, CH-1211 Geneva 4, Switzerland*
[19]*Glasgow University, Glasgow G12 8QQ, United Kingdom*
[20]*Harvard University, Cambridge, Massachusetts 02138, USA*
[21]*Division of High Energy Physics, Department of Physics, University of Helsinki, FIN-00014, Helsinki, Finland; Helsinki Institute of Physics, FIN-00014, Helsinki, Finland*
[22]*University of Illinois, Urbana, Illinois 61801, USA*
[23]*The Johns Hopkins University, Baltimore, Maryland 21218, USA*
[24]*Institut für Experimentelle Kernphysik, Karlsruhe Institute of Technology, D-76131 Karlsruhe, Germany*
[25]*Center for High Energy Physics: Kyungpook National University, Daegu 702-701, Korea; Seoul National University, Seoul 151-742, Korea; Sungkyunkwan University, Suwon 440-746, Korea; Korea Institute of Science and Technology Information, Daejeon 305-806, Korea; Chonnam National University, Gwangju 500-757, Korea; Chonbuk National University, Jeonju 561-756, Korea; Ewha Womans University, Seoul, 120-750, Korea*
[26]*Ernest Orlando Lawrence Berkeley National Laboratory, Berkeley, California 94720, USA*
[27]*University of Liverpool, Liverpool L69 7ZE, United Kingdom*
[28]*University College London, London WC1E 6BT, United Kingdom*
[29]*Centro de Investigaciones Energeticas Medioambientales y Tecnologicas, E-28040 Madrid, Spain*
[30]*Massachusetts Institute of Technology, Cambridge, Massachusetts 02139, USA*
[31]*University of Michigan, Ann Arbor, Michigan 48109, USA*
[32]*Michigan State University, East Lansing, Michigan 48824, USA*
[33]*Institution for Theoretical and Experimental Physics, ITEP, Moscow 117259, Russia*
[34]*University of New Mexico, Albuquerque, New Mexico 87131, USA*
[35]*The Ohio State University, Columbus, Ohio 43210, USA*
[36]*Okayama University, Okayama 700-8530, Japan*
[37]*Osaka City University, Osaka 558-8585, Japan*
[38]*University of Oxford, Oxford OX1 3RH, United Kingdom*
[39]*Istituto Nazionale di Fisica Nucleare, Sezione di Padova, [jj]University of Padova, I-35131 Padova, Italy*
[40]*University of Pennsylvania, Philadelphia, Pennsylvania 19104, USA*
[41]*Istituto Nazionale di Fisica Nucleare Pisa, [kk]University of Pisa, [ll]University of Siena, [mm]Scuola Normale Superiore, I-56127 Pisa, Italy, [nn]INFN Pavia, I-27100 Pavia, Italy, [oo]University of Pavia, I-27100 Pavia, Italy*
[42]*University of Pittsburgh, Pittsburgh, Pennsylvania 15260, USA*
[43]*Purdue University, West Lafayette, Indiana 47907, USA*
[44]*University of Rochester, Rochester, New York 14627, USA*
[45]*The Rockefeller University, New York, New York 10065, USA*
[46]*Istituto Nazionale di Fisica Nucleare, Sezione di Roma 1, [pp]Sapienza Università di Roma, I-00185 Roma, Italy*
[47]*Mitchell Institute for Fundamental Physics and Astronomy, Texas A&M University, College Station, Texas 77843, USA*
[48]*Istituto Nazionale di Fisica Nucleare Trieste, [qq]Gruppo Collegato di Udine, [rr]University of Udine, I-33100 Udine, Italy, [ss]University of Trieste, I-34127 Trieste, Italy*
[49]*University of Tsukuba, Tsukuba, Ibaraki 305, Japan*
[50]*Tufts University, Medford, Massachusetts 02155, USA*
[51]*University of Virginia, Charlottesville, Virginia 22906, USA*

[52]*Waseda University, Tokyo 169, Japan*
[53]*Wayne State University, Detroit, Michigan 48201, USA*
[54]*University of Wisconsin, Madison, Wisconsin 53706, USA*
[55]*Yale University, New Haven, Connecticut 06520, USA*
(Dated: September 16, 2014)

Differential cross sections for the production of Z bosons or off-shell photons γ^* in association with jets are measured in proton-antiproton collisions at center-of-mass energy $\sqrt{s} = 1.96$ TeV using the full data set collected with the Collider Detector at Fermilab in Tevatron Run II, and corresponding to 9.6 fb^{-1} of integrated luminosity. Results include first measurements at CDF of differential cross sections in events with a Z/γ^* boson and three or more jets, the inclusive cross section for production of Z/γ^* and four or more jets, and cross sections as functions of various angular observables in lower jet-multiplicity final states. Measured cross sections are compared to several theoretical predictions.

I. INTRODUCTION

Studies of the production of jets in association with a Z/γ^* boson, henceforth referred to as Z/γ^*+jets processes, are central topics in hadron collider physics. Differential cross section measurements provide stringent tests for perturbative quantum chromodynamics (QCD) predictions [1]. In addition, Z/γ^*+jets production is a background to many rare standard model (SM) processes, such as Higgs-boson production, and searches for non-SM physics. Dedicated measurements can help to improve the theoretical modeling of Z/γ^*+jets production.

Differential cross sections have been previously measured in proton-antiproton collisions by the CDF [2] and D0 [3] collaborations as functions of several variables, including the jet transverse momentum, the jet rapidity, and various angular observables. These measurements are in qualitative agreement with predictions from perturbative QCD at the next-to-leading order (NLO) expansion in the strong-interaction coupling, but are limited by the small number of events with high multiplicity of jets. Recently, measurements have also been published by the ATLAS [4] and CMS [5] collaborations in proton-proton collisions at the LHC, since the understanding of these SM processes is essential in the search for non-SM physics at the LHC.

In this article, measurements of differential cross sections for Z/γ^*+jets production are presented, using the full data sample of proton-antiproton collisions collected with the CDF II detector in Run II of the Tevatron Collider, which corresponds to 9.6 fb^{-1} of integrated luminosity. The results include differential cross sections as functions of jet transverse momentum, p_{T}, and rapidity, y [6], extended for the first time at CDF to the $Z/\gamma^*+\geqslant 3$ jets final state; the total cross section as a function of jet multiplicity up to four jets; and several differential distributions for events with a Z/γ^* boson and at least one or two jets. Measurements are compared to NLO [7, 8] and approximate next-to-next-to-leading order (NNLO) perturbative QCD predictions [9], to NLO QCD predictions including NLO electroweak corrections [10], and to distributions from various Monte Carlo (MC) generators that use parton showers interfaced with fixed-order calculations [11, 12].

This paper is organized as follows: Section II contains a brief description of the CDF II detector. The data sample and the event selection are presented in Sec. III. The MC samples used across the analysis are listed in Sec. IV. The estimation of the background contributions is described in Sec. V. The unfolding procedure is explained in Sec. VI. The systematic uncertainties are addressed in Sec. VII. The theoretical predictions are described in Sec. VIII. The measured differential cross sections are shown and discussed in Sec. IX. Section X summarizes the results.

* Deceased
† With visitors from [a]University of British Columbia, Vancouver, BC V6T 1Z1, Canada, [b]Istituto Nazionale di Fisica Nucleare, Sezione di Cagliari, 09042 Monserrato (Cagliari), Italy, [c]University of California Irvine, Irvine, CA 92697, USA, [d]Institute of Physics, Academy of Sciences of the Czech Republic, 182 21, Czech Republic, [e]CERN, CH-1211 Geneva, Switzerland, [f]Cornell University, Ithaca, NY 14853, USA, [g]University of Cyprus, Nicosia CY-1678, Cyprus, [h]Office of Science, U.S. Department of Energy, Washington, DC 20585, USA, [i]University College Dublin, Dublin 4, Ireland, [j]ETH, 8092 Zürich, Switzerland, [k]University of Fukui, Fukui City, Fukui Prefecture, Japan 910-0017, [l]Universidad Iberoamericana, Lomas de Santa Fe, México, C.P. 01219, Distrito Federal, [m]University of Iowa, Iowa City, IA 52242, USA, [n]Kinki University, Higashi-Osaka City, Japan 577-8502, [o]Kansas State University, Manhattan, KS 66506, USA, [p]Brookhaven National Laboratory, Upton, NY 11973, USA, [q]Queen Mary, University of London, London, E1 4NS, United Kingdom, [r]University of Melbourne, Victoria 3010, Australia, [s]Muons, Inc., Batavia, IL 60510, USA, [t]Nagasaki Institute of Applied Science, Nagasaki 851-0193, Japan, [u]National Research Nuclear University, Moscow 115409, Russia, [v]Northwestern University, Evanston, IL 60208, USA, [w]University of Notre Dame, Notre Dame, IN 46556, USA, [x]Universidad de Oviedo, E-33007 Oviedo, Spain, [y]CNRS-IN2P3, Paris, F-75205 France, [z]Universidad Tecnica Federico Santa Maria, 110v Valparaiso, Chile, [aa]The University of Jordan, Amman 11942, Jordan, [bb]Universite catholique de Louvain, 1348 Louvain-La-Neuve, Belgium, [cc]University of Zürich, 8006 Zürich, Switzerland, [dd]Massachusetts General Hospital, Boston, MA 02114 USA, [ee]Harvard Medical School, Boston, MA 02114 USA, [ff]Hampton University, Hampton, VA 23668, USA, [gg]Los Alamos National Laboratory, Los Alamos, NM 87544, USA, [hh]Università degli Studi di Napoli Federico I, I-80138 Napoli, Italy

II. THE CDF II DETECTOR

The CDF II detector, described in detail in Ref. [13], is composed of a tracking system embedded in a 1.4 T magnetic field, surrounded by electromagnetic and hadronic calorimeters and muon spectrometers. The CDF experiment uses a cylindrical coordinate system in which the z axis lies along the proton beam direction, ϕ is the azimuthal angle, and θ is the polar angle, which is often expressed as pseudorapidity $\eta = -\ln[\tan(\theta/2)]$. The tracking system includes a silicon microstrip detector [14] covering a pseudorapidity range of $|\eta| < 2$, which provides precise three-dimensional reconstruction of charged-particle trajectories (tracks). The silicon detector is surrounded by a 3.1 m long open-cell drift chamber [15], which covers a pseudorapidity range $|\eta| < 1$, providing efficient pattern recognition and accurate measurement of the momentum of charged particles. The calorimeter system is arranged in a projective-tower geometry and measures energies of photons and electrons in the $|\eta| < 3.6$ range. The electromagnetic calorimeter [16, 17] is a lead-scintillator sampling calorimeter, which also contains proportional chambers at a depth corresponding approximately to the maximum intensity of electron showers. The hadronic calorimeter [18] is an iron-scintillator sampling calorimeter. The muon detectors [19], located outside the calorimeters, consist of drift chambers and scintillation counters covering a pseudorapidity range of $|\eta| < 1.0$. Finally, the luminosity is computed from the rate of inelastic $p\bar{p}$ collisions determined by the Cherenkov counters [20] located close to the beam pipe.

III. DATA SAMPLE AND EVENT SELECTION

The data sample consists of $Z/\gamma^* \to e^+e^-$ and $Z/\gamma^* \to \mu^+\mu^-$ + jets candidate events, which have been collected using a three-level online event selection system (trigger) [21] between February 2002 and September 2011. In the electron channel, the trigger requires a central ($|\eta| \leqslant 1$) electromagnetic calorimeter cluster with $E_{\rm T} \geqslant 18$ GeV matched to a charged particle with $p_{\rm T} \geqslant 9$ GeV/c. In the analysis, $Z/\gamma^* \to e^+e^-$ events are selected by requiring two central electrons with $E_{\rm T} \geqslant 25$ GeV and reconstructed invariant mass in the range $66 \leqslant M_{ee} \leqslant 116$ GeV/c^2. Details on the electron identification requirements are given in Ref. [13]. In the muon channel, the trigger requires a signal in the muon detectors associated with a charged particle reconstructed in the drift chamber with $|\eta| \leqslant 1$ and $p_{\rm T} \geqslant 18$ GeV/c. In the analysis, $Z/\gamma^* \to \mu^+\mu^-$ events are selected by requiring two reconstructed muons of opposite electric charge with $|\eta| \leqslant 1$ and $p_{\rm T} \geqslant 25$ GeV/c, and reconstructed invariant mass in the range $66 \leqslant M_{\mu\mu} \leqslant 116$ GeV/c^2. Quality requirements are applied to the tracks in order to reject misidentified muons, and all the muon candidates are required to to be associated with an energy deposit in the calorimeter consistent with a minimum ionizing particle. More details on the muon reconstruction and identification can be found in Ref. [13].

In addition to a Z boson candidate, one or more jets with $p_{\rm T} \geqslant 30$ GeV/c and rapidity $|y| \leqslant 2.1$ are required. Jets are reconstructed using the midpoint algorithm [22] in a cone of radius $R = 0.7$ [23]. Calorimeter towers are clustered if the energy deposits correspond to a transverse energy larger than 0.1 GeV [24] and used as seeds if larger than 1 GeV. Towers associated with reconstructed electrons and muons are excluded. A split-merge procedure is used, which merges a pair of cones if the fraction of the softer cone's transverse momentum shared with the harder cone is above a given threshold; otherwise the shared calorimeter towers are assigned to the cone to which they are closer. The split-merge threshold is set to 0.75. Jet four-momenta are evaluated by adding the four-momenta of the towers according to the E-scheme, $p^{\mu}_{\rm jet} = \sum p^{\mu}_{\rm towers}$, described in Ref. [25]. With such a recombination scheme, jets are in general massive, and in order to study the jet kinematic properties, the variables $p_{\rm T}$ and y are used, which account for the difference between E and p due to the jet mass. Since the jet transverse momentum measured by the calorimeter, $p_{\rm T,cal}$, is affected by instrumental effects, an average correction [26] is applied to $p_{\rm T,cal}$. These effects, mainly due to the noncompensating nature of the calorimeter and the presence of inactive material, are of the order of 30% for $p_{\rm T,cal}$ around 40 GeV/c and reduce to about 11% for high $p_{\rm T,cal}$ jets. A further correction is applied to account for the energy contributions to jets from multiple $p\bar{p}$ interactions, but no modification is made to account for underlying-event contributions or fragmentation effects. The requirement of $p_{\rm T} \geqslant 30$ GeV/c is applied to the corrected jet transverse momentum. Events are selected if the leptons are separated from the selected jets by $\Delta R_{\ell-{\rm jet}} \geqslant 0.7$ [27].

IV. MONTE CARLO SIMULATION

Samples of $Z/\gamma^* \to e^+e^-$ + jets, $Z/\gamma^* \to \mu^+\mu^-$ + jets, and $Z/\gamma^* \to \tau^+\tau^-$ + jets events are generated using ALPGEN v2.14 [11] interfaced to PYTHIA 6.4.25 [28] for the parton shower, with CTEQ5L parton distribution functions (PDF) [29] and using the set of *tuning* parameters denoted as Tune Perugia 2011 [30]. The MLM matching procedure [31] is applied to avoid double-counting of processes between the matrix-element calculations and the parton-shower algorithm of PYTHIA. In addition, samples of $t\bar{t}$, associated production of W and Z bosons (WW, WZ, ZZ), and inclusive Z/γ^* production are generated using PYTHIA v6.2 with the same PDF set and Tune A [32]. All the samples are passed through a full CDF II detector simulation based on GEANT [33], where the GFLASH [34] package is used for parametrization of the energy deposition in the calorimeters, and corrected to account for differences between data and simulation in the trigger selection and lepton identification efficiencies. The electron $E_{\rm T}$ and the muon $p_{\rm T}$ scale and resolution are corrected to match the dilepton invariant mass distributions $M_{\ell\ell}$ observed in the data in the region $84 \leqslant M_{\ell\ell} \leqslant 98$ GeV/c^2. Simulated Z/γ^* + jets samples are also reweighted with respect to the number of multiple $p\bar{p}$ interactions in the same bunch crossing so as to have the same instantaneous luminosity profile of the data. The MC samples are used to determine background contributions and derive the unfolding correction factors de-

scribed in Sec. VI.

V. BACKGROUND CONTRIBUTIONS

The selected sample of $Z/\gamma^* + \text{jets}$ data events is expected to include events from various background processes. The largest background contributions come from pair production of W and Z bosons, WW, WZ, ZZ, and top-antitop quarks, $t\bar{t}$; a smaller contribution comes from $Z/\gamma^* \to \tau^+\tau^- + \text{jets}$ events. Inclusive jets and $W + \text{jets}$ events contribute to the background if one or more jets are misidentified as electrons or muons. Various strategies are used to estimate the background contributions. In the $Z/\gamma^* \to e^+e^-$ channel, a data-driven method is used to estimate the inclusive jets and $W + \text{jets}$ background contribution. First, the probability for a jet to pass the electron selection requirements is evaluated using an inclusive jet data sample. This is denoted as *fake* rate and is parametrized as a function of the jet transverse energy. The fake rate is applied to jets from a sample of events with one reconstructed electron: for each event, all the possible electron-jet combinations are considered as Z/γ^* candidates, the jet transverse energy is corrected to match on average the corresponding electron energy, and all the electron-jet pairs that fulfill the selection requirements are weighted with the corresponding fake rate associated with the jet, and used to estimate the background rate for each observed distribution.

In the muon channel, the $W + \text{jets}$ and inclusive jets processes constitute a source of background if a track inside a jet is identified as a muon. To estimate this background contribution, events containing muon pairs are reconstructed following the analysis selection but requiring the charge of the two muons to have the same electric charge.

The other background contributions, originating from $t\bar{t}$, associated production of W and Z bosons (WW, WZ, ZZ), and $Z/\gamma^* \to \tau^+\tau^-$ + jets, are estimated with simulated samples. The $t\bar{t}$ sample is normalized according to the approximate NNLO cross section [35], the WW, WZ and ZZ samples are normalized according to the NLO cross sections [36], and the $Z/\gamma^* \to \tau^+\tau^- + \text{jets}$ sample is normalized according to the Z inclusive NNLO cross section [13]. The total background varies from about 2% to 6% depending on jet multiplicity as shown in Table I, which reports the sample composition per jet-multiplicity bin in the electron and muon channels.

Figure 1 shows the invariant mass distribution for $Z/\gamma^* + \geqslant 1$ jet events in the electron and muon decay channels. The region outside the mass range used in the analysis contains a larger fraction of background processes. Table II shows the comparison between data and $Z/\gamma^* + \text{jets}$ signal plus background prediction for $Z/\gamma^* + \geqslant 1$ jet events in the low- and high-mass regions $40 \leqslant M_{\ell\ell} < 66$ GeV/c^2 and $116 < M_{\ell\ell} \leqslant 145$ GeV/c^2, respectively. The good agreement between data and expectation supports the method used to estimate the sample composition.

TABLE I. Estimated background contributions, background systematic uncertainties, and data yield for (a) $Z/\gamma^* \to e^+e^- + \geqslant N_{\text{jets}}$ and (b) $Z/\gamma^* \to \mu^+\mu^- + \geqslant N_{\text{jets}}$ channels, with the number of jets $N_{\text{jets}} \geqslant 1, 2, 3$, and 4.

$Z/\gamma^* \to e^+e^-$ + jets	Estimated events			
Backgrounds	$\geqslant 1$ jet	$\geqslant 2$ jets	$\geqslant 3$ jets	$\geqslant 4$ jets
QCD, W + jets	25.9 ± 3.9	4.0 ± 0.6	0.6 ± 0.1	$\leqslant 0.1$
WW, ZZ, ZW	119 ± 36	43 ± 13	4.2 ± 1.3	0.3 ± 0.1
$t\bar{t}$	45 ± 13	25.4 ± 7.6	2.9 ± 0.9	0.2 ± 0.1
$Z/\gamma^* \to \tau^+\tau^-$ + jets	7.2 ± 2.2	0.5 ± 0.1	< 0.1	< 0.1
Total background	197 ± 38	73 ± 15	7.8 ± 1.5	0.7 ± 0.1
Data	12910	1451	137	13

(a)

$Z/\gamma^* \to \mu^+\mu^-$ + jets	Estimated events			
Backgrounds	$\geqslant 1$ jet	$\geqslant 2$ jets	$\geqslant 3$ jets	$\geqslant 4$ jets
QCD, W + jets	51 ± 51	18 ± 18	3 ± 3	1 ± 1
WW, ZZ, ZW	190 ± 57	69 ± 21	6.7 ± 2.0	0.5 ± 0.2
$t\bar{t}$	68 ± 21	38 ± 12	4.5 ± 1.3	0.5 ± 0.1
$Z/\gamma^* \to \tau^+\tau^-$ + jets	9.4 ± 2.8	1.2 ± 0.3	$\leqslant 0.1$	< 0.1
Total background	318 ± 79	126 ± 30	14.3 ± 3.8	2.0 ± 1.0
Data	19578	2247	196	13

(b)

VI. UNFOLDING

Measured cross sections need to be corrected for detector effects in order to be compared to the theoretical predictions. The comparison between data and predictions is performed at the particle level, which refers to experimental signatures reconstructed from quasi-stable (lifetime greater than 10 ps) and color-confined final-state particles including hadronization and underlying-event contributions, but not the contribution of multiple $p\bar{p}$ interactions in the same bunch crossing [37]. Detector-level cross sections are calculated by subtracting the estimated background from the observed events and dividing by the integrated luminosity. Measured cross sections are unfolded from detector level to particle level with a bin-by-bin procedure. For each bin of a measured observable α, the ALPGEN+PYTHIA $Z/\gamma^* \to e^+e^-$ + jets and $Z/\gamma^* \to \mu^+\mu^-$ + jets MC samples are used to evaluate the unfolding factors, which are defined as $U_\alpha = \frac{d\sigma_{\text{p}}^{\text{MC}}}{d\alpha} / \frac{d\sigma_{\text{d}}^{\text{MC}}}{d\alpha}$, where $\sigma_{\text{p}}^{\text{MC}}$ and $\sigma_{\text{d}}^{\text{MC}}$ are the simulated particle-level and detector-level cross sections, respectively. Measured particle level cross sections are evaluated as $\frac{d\sigma_{\text{p}}}{d\alpha} = \frac{d\sigma_{\text{d}}}{d\alpha} \cdot U_\alpha$, where σ_{d} is the detector-level measured cross section. The simulated samples used for the unfolding are validated by comparing measured

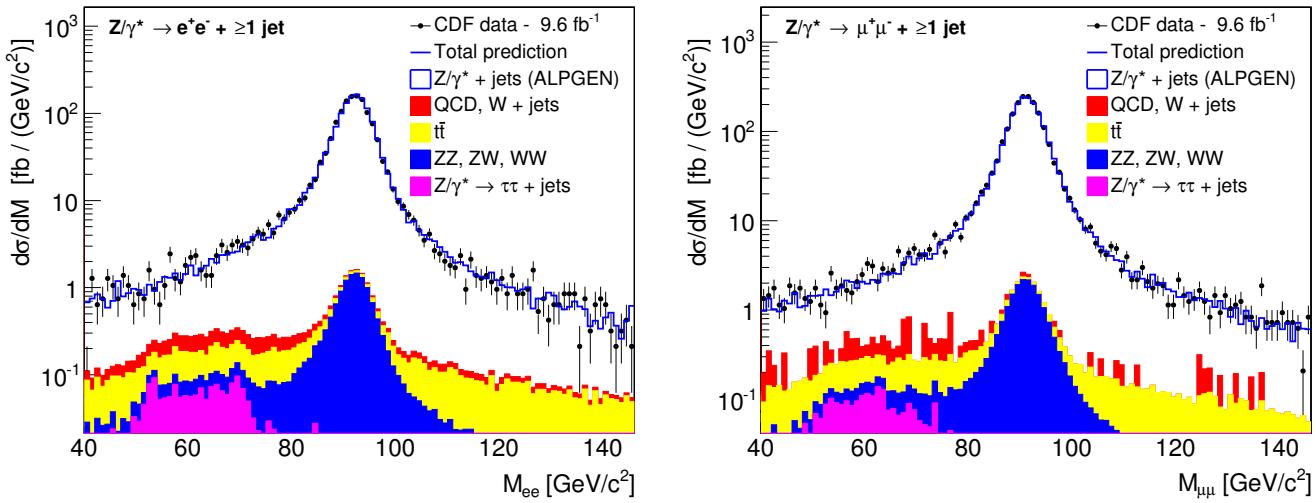

(a) (b)

FIG. 1. Dilepton invariant mass distributions for events with at least one jet in the (a) $Z/\gamma^* \to e^+e^-$ and (b) $Z/\gamma^* \to \mu^+\mu^-$ channels. Observed number of events divided by the integrated luminosity (black dots) are compared to the MC expectation (solid blue line), including signal and backgrounds contributions (filled histograms).

TABLE II. Estimated background events and Z/γ^* + jets MC prediction compared to the data in the low- and high-mass regions outside the mass range used in the analysis, for $Z/\gamma^* \to e^+e^-$ + $\geqslant 1$ jet and $Z/\gamma^* \to \mu^+\mu^-$ + $\geqslant 1$ jet events. Invariant mass ranges are given in GeV/c^2. Background systematic uncertainties and statistical uncertainties of the Z/γ^* + jets MC prediction are shown.

	$Z/\gamma^* \to e^+e^- + \geq 1$ jet		$Z/\gamma^* \to \mu^+\mu^- + \geq 1$ jet	
Backgrounds	$40 \leqslant M_{ee} < 66$	$116 < M_{ee} \leqslant 145$	$40 \leqslant M_{\mu\mu} < 66$	$116 < M_{\mu\mu} \leqslant 145$
QCD, W + jets	15.9 ± 2.4	2.9 ± 0.4	37 ± 37	8 ± 8
WW, ZZ, ZW	5.2 ± 1.6	3.2 ± 1.0	7.5 ± 2.3	4.6 ± 1.4
$t\bar{t}$	19.7 ± 5.9	15.6 ± 4.7	30.1 ± 9.0	22.4 ± 6.7
$Z/\gamma^* \to \tau^+\tau^-$ + jets	10.9 ± 3.3	0.3 ± 0.1	17.5 ± 5.2	0.3 ± 0.1
Total background	51.7 ± 7.3	21.9 ± 4.8	92 ± 39	35 ± 11
Z/γ^* + jets (ALPGEN)	238.6 ± 6.5	196.7 ± 5.6	335.4 ± 7.2	289.0 ± 6.4
Total prediction	290.3 ± 9.8	218.6 ± 7.3	428 ± 39	324 ± 12
Data	312	226	486	334

and predicted cross sections at detector level. The unfolding factors account for $Z/\gamma^* \to \ell^+\ell^-$ reconstruction efficiency, particle detection, and jet reconstruction in the calorimeter. Unfolding factors are typically around 2.5 (1.7) in value and vary between 2.3 (1.6) at low $p_{\rm T}$ and 3 (2) at high $p_{\rm T}$ for the $Z/\gamma^* \to e^+e^-$ ($Z/\gamma^* \to \mu^+\mu^-$) channel.

At particle level, radiated photons are recombined with leptons following a scheme similar to that used in Ref. [10]. A photon and a lepton from $Z/\gamma^* \to \ell^+\ell^-$ decays are recombined when $\Delta R_{\gamma-\ell} \leqslant 0.1$. If both charged leptons in the final state are close to a photon, the photon is recombined with the lepton with the smallest $\Delta R_{\gamma-\ell}$. Photons that are not recombined to leptons are included in the list of particles for the jet clustering. With such a definition, photons are clustered into jets at the particle level, and $Z/\gamma^* + \gamma$ production is included in the definition of Z/γ^* + jets. The contribution of the $Z/\gamma^* + \gamma$ process to the Z/γ^* + jets cross section is at the percent level, and taken into account in the PYTHIA simulation through photon initial- (ISR) and final-state radiation (FSR).

Reconstruction of experimental signatures and kinematic requirements applied at particle level establish the measurement definition. Requirements applied at the detector level are also applied to jets and leptons at the particle level so as to reduce the uncertainty of the extrapolation of the measured cross section. Jets are reconstructed at particle level in the simulated sample with the midpoint algorithm in a cone of radius $R = 0.7$, the split-merge threshold set to 0.75, and using as seeds particles with $p_{\rm T} \geqslant 1$ GeV/c. The measured cross sections are defined in the kinematic region $66 \leqslant M_{\ell\ell} \leqslant 116$ GeV/c^2, $|\eta^\ell| \leqslant 1$, $p_{\rm T}^\ell \geqslant 25$ GeV/c ($\ell = e$, μ),

$p_{\rm T}^{\rm jet} \geqslant 30$ GeV/c, $|y^{\rm jet}| \leqslant 2.1$, and $\Delta R_{\ell-{\rm jet}} \geqslant 0.7$.

VII. SYSTEMATIC UNCERTAINTIES

All significant sources of systematic uncertainties are studied. The main systematic uncertainty of the $Z/\gamma^* \to \ell^+\ell^-$ + jets measurement is due to the jet-energy-scale correction. The jet-energy scale is varied according to Ref. [26]. Three sources of systematic uncertainty are considered: the absolute jet-energy scale, multiple $p\bar{p}$ interactions, and the η-dependent calorimeter response. The absolute jet-energy scale uncertainty depends on the response of the calorimeter to individual particles and on the accuracy of the simulated model for the particle multiplicity and $p_{\rm T}$ spectrum inside a jet. This uncertainty significantly affects observables involving high-$p_{\rm T}$ jets and high jet multiplicity. The jet-energy uncertainty related to multiple $p\bar{p}$ interactions arises from inefficiency in the reconstruction of multiple interaction vertices, and mainly affects jets with low $p_{\rm T}$ and high rapidity, and events with high jet multiplicity. The η-dependent uncertainty accounts for residual discrepancies between data and simulation after the calorimeter response is corrected for the dependence on η.

Trigger efficiency and lepton identification uncertainties are of the order of 1% and give small contributions to the total uncertainty.

A 30% uncertainty is applied to the MC backgrounds yield estimation, to account for missing higher-order corrections on the cross-section normalizations [2]. In the $Z/\gamma^* \to e^+e^-$ channel, a 15% uncertainty is assigned to the data-driven QCD and $W+$jets background yield estimation, to account for the statistical and systematic uncertainty of the fake-rate parametrization. In the $Z/\gamma^* \to \mu^+\mu^-$ channel a 100% uncertainty is applied to the subtraction of QCD and $W+$jets background, which accounts for any difference between the observed same-charge yield and the expected opposite-charge background contribution. The impact of both sources to the uncertainties of the measured cross sections is less than 2%. The primary vertex acceptance is estimated by fitting the beam luminosity as a function of z using minimum bias data, the uncertainty on the primary vertex acceptance is approximately 1%. Finally, the luminosity estimation has an uncertainty of 5.8% which is applied to the measurements [38]. As examples, systematic uncertainties as functions of inclusive jet $p_{\rm T}$ in the $Z/\gamma^* \to e^+e^-$ channel and inclusive jet rapidity in the $Z/\gamma^* \to \mu^+\mu^-$ channel are shown in Fig. 2, the corresponding systematic uncertainties as functions of inclusive jet $p_{\rm T}$ in the $Z/\gamma^* \to \mu^+\mu^-$ channel and inclusive jet rapidity in the $Z/\gamma^* \to e^+e^-$ channel have similar trends.

VIII. THEORETICAL PREDICTIONS

Measured Z/γ^*+jets differential cross sections are compared to several theoretical predictions such as NLO perturbative QCD calculations evaluated with MCFM [7] and BLACKHAT+SHERPA [8], approximate NNLO LOOPSIM+MCFM predictions [9], perturbative NLO QCD predictions including NLO electroweak corrections [10], and to generators based on LO matrix element (ME) supplemented by parton showers (PS), like ALPGEN+PYTHIA [11, 28], and NLO generators interfaced to PS as POWHEG+PYTHIA [12]. For the LOOPSIM+MCFM predictions, the notation $\bar{\rm n}^p{\rm N}^q$LO introduced in Ref. [9] is used, which denotes an approximation to the N^{p+q}LO result in which the q lowest loop contributions are evaluated exactly, whereas the p highest loop contributions are evaluated with the LOOPSIM approximation; according to such a notation, the approximate NNLO LOOPSIM+MCFM predictions are denoted with $\bar{\rm n}$NLO. The NLO MCFM predictions are available for final states from Z/γ^* production in association with one or more, and two or more jets, LOOPSIM+MCFM only for the $Z/\gamma^*+\geqslant 1$ jet final state, NLO BLACKHAT+SHERPA for jet multiplicity up to $Z/\gamma^*+\geqslant 3$ jets, and POWHEG+PYTHIA predictions are available for all jet multiplicities but have NLO accuracy only for $Z/\gamma^*+\geqslant 1$ jet. The ALPGEN LO calculation is available for jet multiplicities up to Z/γ^* + 6 jets but, for the current comparison, the calculation is restricted to up to $Z/\gamma^*+\geqslant 4$ jets. Electroweak corrections at NLO are available for the $Z/\gamma^*+\geqslant 1$ jet final state. Table III lists the theoretical predictions which are compared to measured cross sections.

The input parameters of the various predictions are chosen to be homogeneous in order to emphasize the difference between the theoretical models. The MSTW2008 [39] PDF sets are used as the default choice in all the predictions. The LO PDF set and one-loop order for the running of the strong-interaction coupling constant α_s are used for the LO MCFM and BLACKHAT+SHERPA predictions; the NLO PDF set and two-loop order for the running of α_s for POWHEG, ALPGEN, NLO MCFM, and NLO BLACKHAT predictions; the NNLO PDF set and three-loop order for the running of α_s for the $\bar{\rm n}$NLO LOOPSIM prediction. The contribution to the NLO MCFM prediction uncertainty due to the PDF is estimated with the MSTW2008NLO PDF set at the 68% confidence level (CL), by using the Hessian method [40]. There are 20 eigenvectors and a pair of uncertainty PDF associated with each eigenvector. The pair of PDF corresponds to positive and negative 68% CL excursions along the eigenvector. The PDF contribution to the prediction uncertainty is the quadrature sum of prediction uncertainties from each uncertainty PDF. The impact of different PDF sets is studied in MCFM, ALPGEN and POWHEG. The variation in the predictions with CTEQ6.6 [41], NNPDF2.1 [42], CT10 [43], and MRST2001 [44] PDF sets is of the same order of the MSTW2008NLO uncertainty. The LHAPDF 5.8.6 library [45] is used to access PDF sets, except in ALPGEN, where PDF sets are provided within the MC program.

The nominal choice [46, 47] for the functional form of the renormalization and factorization scales is $\mu_0 = \hat{H}_T/2 = \frac{1}{2}\left(\sum_j p_T^j + p_T^{\ell^+} + p_T^{\ell^-}\right)$ [48], where the index j runs over the partons in the final state. An exception to this default choice is the ALPGEN prediction, which uses $\mu_0 = \sqrt{m_Z^2 + \sum_j p_T^j}$; the difference with respect to $\mu_0 = \hat{H}_T/2$ was found to be negligible [49]. The factorization and renormalization scales

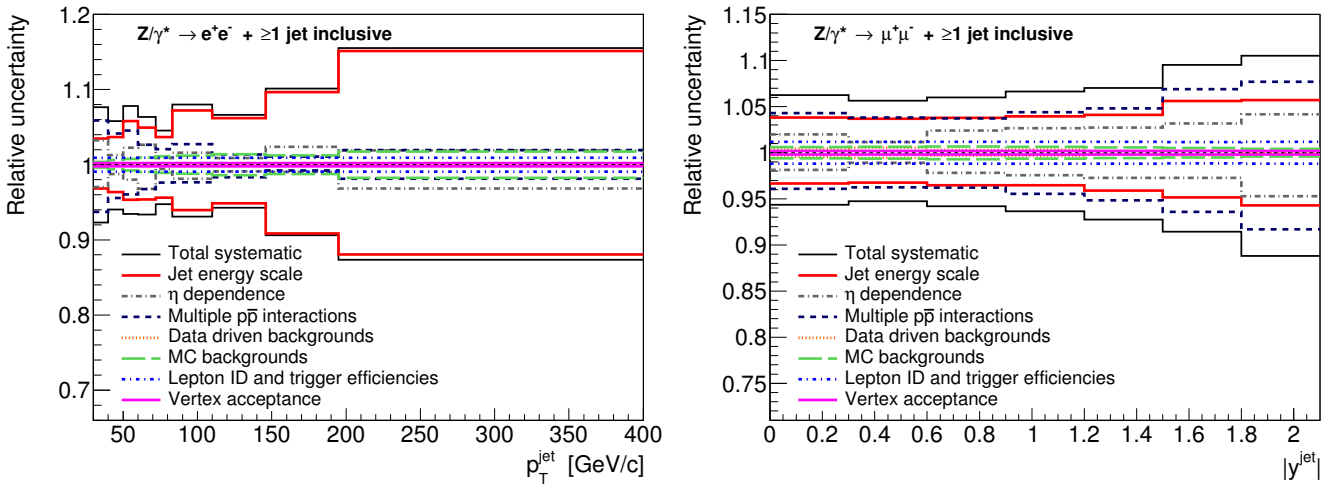

(a) (b)

FIG. 2. Relative systematic uncertainties as functions of (a) inclusive jet p_{T} in the $Z/\gamma^* \to e^+e^-$ channel and (b) inclusive jet rapidity in the $Z/\gamma^* \to \mu^+\mu^-$ channel, for events with $Z/\gamma^* + \geqslant 1$ jet.

TABLE III. Summary of the theoretical predictions compared to the measured cross sections. The order of the expansion in the strong-interaction coupling (QCD order), the order of the expansion in the fine-structure constant (EW order), the matching to a parton shower, and the available jet multiplicities in $Z/\gamma^* +$jets production are shown for each prediction.

Prediction	QCD order	EW order	Parton shower	Jets multiplicity
MCFM	LO/NLO	LO	no	$Z/\gamma^* + \geqslant 1$ and 2 jets
BLACKHAT+SHERPA	LO/NLO	LO	no	$Z/\gamma^* + \geqslant 1, 2$, and 3 jets
LOOPSIM+MCFM	$\overline{\text{n}}$NLO	LO	no	$Z/\gamma^* + \geqslant 1$ jet
NLO QCD $\otimes$ NLO EW	NLO	NLO	no	$Z/\gamma^* + \geqslant 1$ jet
ALPGEN+PYTHIA	LO	LO	yes	$Z/\gamma^* + \geqslant 1, 2, 3$, and 4 jets
POWHEG+PYTHIA	NLO	LO	yes	$Z/\gamma^* + \geqslant 1, 2, 3$, and 4 jets

are varied simultaneously between half and twice the nominal value μ_0, and the corresponding variations in the cross sections are considered as an uncertainty of the prediction. This is the largest uncertainty associated with the theoretical models, except for the ALPGEN+PYTHIA prediction, where the largest uncertainty is associated with the variation of the renormalization scale using the Catani, Krauss, Kuhn, Webber (CKKW) scale-setting procedure [50]. In the ALPGEN prediction, the value of the QCD scale, Λ_{QCD}, and the running order of the strong-interaction coupling constant in the CKKW scale-setting procedure, α_s^{CKKW}, are set to $\Lambda_{QCD} = 0.26$ and one loop, respectively [51]. These settings match the corresponding values of Λ_{QCD} and the running order of α_s for ISR and FSR of the PYTHIA Tune Perugia 2011. The variation of the CKKW renormalization scale is introduced together with an opposite variation of Λ_{QCD} in the PYTHIA tune. Simultaneous variations of the renormalization and factorization scales for the matrix element generation in ALPGEN were found to be smaller than the variation of the CKKW scale [49]. The differences with respect to the previously used Tune A and Tune DW [52] are studied, with the α_s-matched setup of Tune Perugia 2011 providing a better modeling of the shape and normalization of the $Z/\gamma^* +$jets differential cross sections. In the case of Tune A and Tune DW, the running of α_s^{CKKW} in ALPGEN and Λ_{QCD} in PYTHIA is determined by the PDF set, which is CTEQ5L in both to avoid mismatch. The POWHEG calculation is performed with the weighted events option, and the Born suppression factor for the reweight is set to 10 GeV/c, following Ref. [12]. Further studies on the impact of different choices of the functional form of the renormalization and factorization scales have been performed in Ref. [49].

In the LO and NLO MCFM predictions, jets are clustered with the native MCFM *cone* algorithm with $R = 0.7$. This is a seedless cone algorithm that follows the jet clustering outlined in Ref. [25]. The split-merge threshold is set to 0.75, and the maximum ΔR separation R_{sep} for two partons to be clustered in the same jet [53], is set to $R_{sep} = 1.3R$ [2]. For the LOOPSIM+MCFM prediction the minimum jet p_{T} for the generation is set to 1 GeV/c, and the jet clustering is performed with the fastjet [54] interface to the SISCone [55] jet algorithm with cone radius $R = 0.7$ and a split-merge threshold of 0.75. The

same parameters and setup for the jet clustering are used in the BLACKHAT+SHERPA calculation, and the predictions are provided by the BLACKHAT authors.

A recently developed MC program allows the calculation of both NLO electroweak and NLO QCD corrections to the $Z/\gamma^*+\geqslant 1$ jet cross sections [10]. In such a prediction, the QCD and electroweak part of the NLO corrections are combined with a factorization ansatz: NLO QCD and electroweak corrections to the LO cross section are evaluated independently and multiplied. Such a combined prediction is referred to as NLO QCD $\otimes$ NLO EW. The prediction is evaluated with the configuration described in Ref. [10], except for the renormalization and factorization scales, which are set to $\mu_0 = \hat{H}_T/2$, and the predictions are provided by the authors.

Fixed-order perturbative QCD predictions need to be corrected for nonperturbative QCD effects in order to compare them with the measured cross sections, including the underlying event associated with multiparton interactions, beam remnants, and hadronization. Another important effect that is not accounted for in the perturbative QCD predictions and needs to be evaluated is the quantum electrodynamics (QED) photon radiation from leptons and quarks. Both ISR and FSR are considered, with the main effect coming from FSR. The inclusion of QED radiation also corrects the Z/γ^*+jets cross sections for the contribution of $Z/\gamma^*+\gamma$ production, which enters the definition of the Z/γ^*+jets particle level used in this measurement. The nonperturbative QCD effects and the QED radiation are estimated with the MC simulation based on the α_s-matched Perugia 2011 configuration of ALPGEN+PYTHIA, where PYTHIA handles the simulation of these effects. To evaluate the corrections, parton-level and particle-level ALPGEN+PYTHIA cross sections are defined: parton-level cross sections are calculated with QED radiation, hadronization, and multiparton interactions disabled in the PYTHIA simulation, whereas these effects are simulated for the particle-level cross sections. Kinematic requirements on leptons and jets and jet-clustering parameters for the parton and particle levels are the same as those used for the measured cross sections, and photons are recombined to leptons in $\Delta R = 0.1$ if radiated photons are present in the final state. The corrections are obtained by evaluating the ratio of the particle-level cross sections over the parton-level cross sections, bin-by-bin for the various measured variables. Figure 3 shows the parton-to-particle corrections as functions of inclusive jet p_{T} and inclusive jet rapidity for $Z/\gamma^*+\geqslant 1$ jet events, with the contributions from QED ISR and FSR radiation, hadronization, and underlying event. The corrections have a moderate dependence on jet multiplicity, as shown in Fig. 4. Figure 5 shows the parton-to-particle corrections evaluated with various tunes of the underlying-event and hadronization model in PYTHIA, namely Tune A [32], Tune DW [52], Tune Perugia 2011 [30], and Tune Z1 [56], and with the ALPGEN+PYTHIA or POWHEG+PYTHIA simulations. The corrections are generally below 10%, and independent of the PYTHIA MC tune and of the underlying matrix-element generator.

The Z/γ^*+jets cross sections are measured using the midpoint algorithm for the reconstruction of the jets in the final state. The midpoint algorithm belongs to the class of iterative cone algorithms. Though they present several experimental advantages, iterative cone algorithms are not infrared and collinear safe, which means that the number of hard jets found by such jet algorithms is sensitive to a collinear splitting or to the addition of a soft emission. In particular the midpoint jet algorithm used in this measurement is infrared unsafe, as divergences appear in a fixed-order calculation for configurations with three hard particles close in phase space plus a soft one, as discussed in Refs. [55, 57]. In order to compare the measured cross sections with a fixed-order prediction, an infrared and collinear safe jet algorithm that is as similar as possible to the midpoint algorithm, is used in the prediction. This is the SISCone algorithm with the same split-merge threshold of 0.75 and the same jet radius $R = 0.7$ of the midpoint algorithm used for the measured cross sections. The additional uncertainty coming from the use of different jet algorithms between data and theory is estimated by comparing the particle-level cross sections for the two jet algorithms. Figure 6 shows the cross section ratios of midpoint and SISCone jet algorithms for inclusive jet p_{T} and rapidity in the $Z/\gamma^*+\geqslant 1$ jet final state. The difference at parton level between SISCone and midpoint is between 2% and 3%. Larger differences between midpoint and SISCone are observed if the underlying event is simulated; however, they do not affect the comparison with fixed-order predictions. Figure 7 shows the same comparison as a function of jet multiplicity. The difference at parton level between midpoint and SISCone is always below 3% and generally uniform.

IX. RESULTS

The differential cross sections of Z/γ^*+jets production in $p\bar{p}$ collisions are measured independently in the $Z/\gamma^* \to e^+e^-$ and $Z/\gamma^* \to \mu^+\mu^-$ decay channels and combined using the best linear unbiased estimate (BLUE) method [58]. The BLUE algorithm returns a weighted average of the measurements taking into account different types of uncertainty and their correlations. Systematic uncertainties related to trigger efficiencies, lepton reconstruction efficiencies, and QCD and $W+$jets background estimation are considered uncorrelated between the two channels; all other contributions are treated as fully correlated.

Inclusive $Z/\gamma^*+\geqslant N_{\mathrm{jets}}$ cross sections are measured for number of jets $N_{\mathrm{jets}} \geqslant 1,2,3$, and 4, various differential cross sections are measured in the $Z/\gamma^*+\geqslant 1$ jet, $Z/\gamma^*+\geqslant 2$ jets, and $Z/\gamma^*+\geqslant 3$ jets final states. Table IV summarizes the measured cross sections.

A. Cross section for the production of a Z/γ^* boson in association with N or more jets

The $Z/\gamma^*+\geqslant N_{\mathrm{jets}}$ production cross sections are measured for N_{jets} up to four and compared to LO and NLO perturbative QCD BLACKHAT+SHERPA, LO-ME+PS ALPGEN+PYTHIA, and NLO+PS POWHEG+PYTHIA predictions. The $Z/\gamma^*+\geqslant 1$ jet cross section is compared also to the

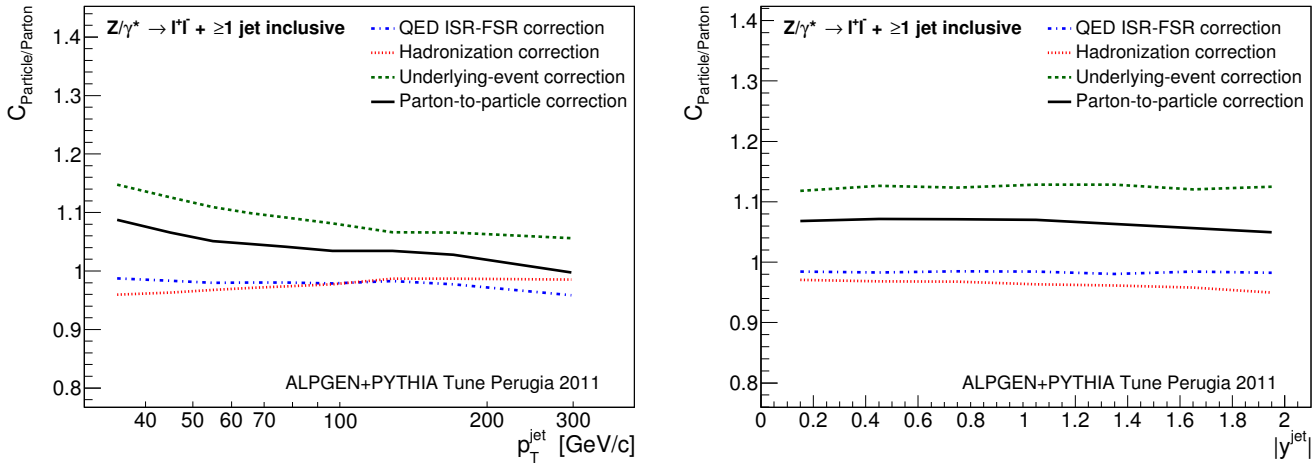

(a) (b)

FIG. 3. Parton-to-particle corrections as functions of (a) inclusive jet p_{T} and (b) inclusive jet rapidity for Z/γ^* + $\geqslant$ 1 jet events. The relative contributions of QED radiation, hadronization, and underlying event are shown.

TABLE IV. Summary of measured cross sections for each $Z/\gamma^* + \geqslant N_{\mathrm{jets}}$ final state.

Final state	Measured quantity (Fig.)
$Z/\gamma^* + \geqslant N_{\mathrm{jets}}$	Inclusive cross section for $N_{\mathrm{jets}} \geqslant 1, 2, 3$, and 4 (8)
$Z/\gamma^* + \geqslant 1$ jet	Leading jet p_{T} (9), inclusive jet p_{T} (10,11), inclusive jet y (12,13), p_{T}^{Z} (14), $\Delta\phi_{Z,\mathrm{jet}}$ (15), $H_{\mathrm{T}}^{\mathrm{jet}}$ (16)
$Z/\gamma^* + \geqslant 2$ jets	*2nd* leading jet p_{T} (17), inclusive-jet y (18), M_{jj} (19), dijet ΔR (20), dijet $\Delta\phi$ (21), dijet Δy (22), $\theta_{Z,jj}$ (23)
$Z/\gamma^* + \geqslant 3$ jets	3rd leading jet p_{T} (24 a), inclusive-jet y (24 b)

$\overline{\mathrm{n}}$NLO LOOPSIM+MCFM prediction. Figure 8 shows the inclusive cross section as a function of jet multiplicity for Z/γ^* + $\geqslant$ 1, 2, 3 and 4 jets. The measured cross section is in general good agreement with all the predictions. The blue dashed bands show the theoretical uncertainty associated with the variation of the renormalization and factorization scales, except for the ALPGEN+PYTHIA prediction, where the band shows the uncertainty associated with the variation of the CKKW renormalization scale. The ALPGEN+PYTHIA LO-ME+PS prediction provides a good model of the measured cross sections, but has large theoretical uncertainty at higher jet multiplicities. The BLACKHAT+SHERPA NLO perturbative QCD prediction shows a reduced scale dependence with respect to the ALPGEN+PYTHIA LO-ME+PS prediction. The POWHEG+PYTHIA NLO+PS prediction has NLO accuracy only for $Z/\gamma^* + \geqslant 1$ jet, but it can be compared to data in all the measured jet multiplicities, where a general good agreement is observed. The LOOPSIM+MCFM $\overline{\mathrm{n}}$NLO prediction is currently available only for $Z/\gamma^* + \geqslant 1$ jet, where it shows a very good agreement with the measured cross section and a reduced scale-variation uncertainty at the level of 5%.

The $Z/\gamma^* + \geqslant 3$ jets BLACKHAT+SHERPA NLO perturbative QCD calculation appears to be approximately 30% lower than data, with the difference covered by the scale-variation uncertainty. Such a difference is not observed in the comparison with LO-ME+PS ALPGEN+PYTHIA and NLO+PS POWHEG+PYTHIA predictions, in agreement with recent measurements using the anti-k_t jet algorithm [4], which do not show any difference with the NLO predictions at high jet multiplicities. The reason of this difference has been found to be related to the different ΔR angular reach [57] between the SISCone and anti-k_t algorithms, and how it is influenced by additional radiation between two hard particles [49]. The difference between data or LO-ME+PS with respect to the NLO prediction in the $Z/\gamma^* + \geqslant 3$ jets final state is explained with the presence of higher-order QCD radiation, which reduces the angular reach of the SISCone algorithm and increases the cross section in this particular configuration.

B. Cross section for the production of a Z/γ^* boson in association with one or more jets

Figures 9 and 10 show the leading-jet and inclusive-jet cross sections differential in p_{T} for $Z/\gamma^* + \geqslant 1$ jet events. All the theoretical predictions are in reasonable agreement with the measured cross sections. The NLO electroweak corrections give a 5% negative contribution in the last Z/γ^* and lead-

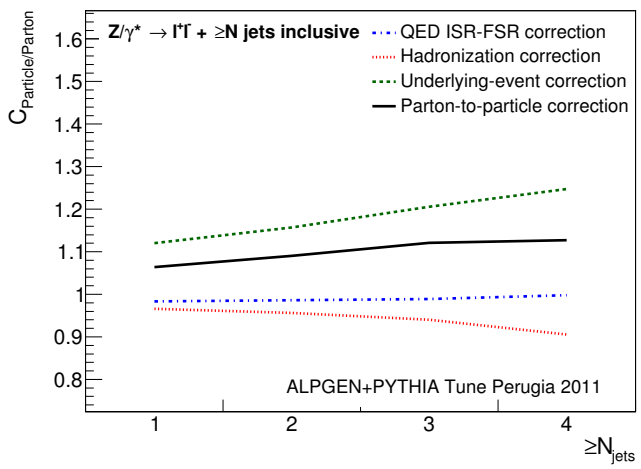

FIG. 4. Parton-to-particle corrections as a function of jet multiplicity. The relative contributions of QED radiation, hadronization, and underlying event are shown.

ing jet p_{T} bin, due to the large Sudakov logarithms that appear in the virtual part of the calculation [10]. The scale-variation uncertainty is quite independent of the jet p_{T} and of the order of $4\% - 6\%$ for the $\bar{\mathrm{n}}$NLO LOOPSIM prediction. Figure 11 shows variations in the MCFM prediction with different values of the strong-interaction coupling constant at the Z boson mass, $\alpha_s(M_Z)$, factorization scale, PDF sets, and choice of the functional form of the factorization and renormalization scales.

Figure 12 shows the inclusive-jet cross sections differential in rapidity for $Z/\gamma^* + \geqslant 1$ jet events. All predictions correctly model this quantity. In the high-rapidity region the measured cross section is higher than predictions; however, the difference is covered by the uncertainty due to the contribution of multiple $p\bar{p}$ interaction. The $\bar{\mathrm{n}}$NLO LOOPSIM+MCFM prediction has the lowest scale-variation theoretical uncertainty, which is of the order of $4\% - 6\%$, and the PDF uncertainty is between 2% and 4%. In the high-rapidity region the ALPGEN prediction is lower than other theoretical models; however, the difference with data is covered by the large CKKW renormalization scale-variation uncertainty of this prediction. Figure 13 shows variations in the MCFM prediction with different values of $\alpha_s(M_Z)$, factorization scale, PDF sets, and choice of the functional form of the factorization and renormalization scales.

Figure 14 shows the production cross section differential in $p_{\mathrm{T}}(Z/\gamma^*)$ for the $Z/\gamma^* + \geqslant 1$ jet final state. The perturbative QCD fixed-order calculations MCFM and LOOPSIM+MCFM fail in describing the region below the 30 GeV/c jet p_{T} threshold, where multiple-jet emission and nonperturbative QCD corrections are significant. The low Z/γ^* p_{T} region is better described by the ALPGEN+PYTHIA and POWHEG+PYTHIA predictions, which include parton shower radiation, and in which the nonperturbative QCD corrections are applied as part of the PYTHIA MC event evolution. In the intermediate Z/γ^* p_{T} region, the ratios of the data over the NLO MCFM, NLO+PS POWHEG+PYTHIA and $\bar{\mathrm{n}}$NLO LOOPSIM+MCFM predictions show a slightly concave shape, which is covered by the scale-variation uncertainty. The NLO electroweak corrections related to the large Sudakov logarithms are negative and of the order of 5% in the last p_{T} bin.

Figure 15 shows the differential cross section as a function of the Z/γ^*-leading jet $\Delta\phi$ variable in $Z/\gamma^* + \geqslant 1$ jet events. The ALPGEN+PYTHIA prediction shows good agreement with the measured cross section in the region $\Delta\phi \geqslant \pi/2$. In the region $\Delta\phi < \pi/2$ the ALPGEN+PYTHIA prediction is lower than the data, with the difference covered by the scale-variation uncertainty. The POWHEG+PYTHIA prediction has very good agreement with the data over all of the Z/γ^*-jet $\Delta\phi$ spectrum, and is affected by smaller scale-variation uncertainty. The difference between the ALPGEN+PYTHIA and POWHEG+PYTHIA predictions is comparable to the experimental systematic uncertainty, which is dominated by the uncertainty from the contribution of multiple $p\bar{p}$ interactions. Hence, the measured cross section cannot be used to distinguish between the two models. The NLO MCFM prediction fails to describe the region $\Delta\phi < \pi/2$ because it does not include the Z/γ^* + 3 jets configuration, whereas $\bar{\mathrm{n}}$NLO LOOPSIM+MCFM, which includes the Z/γ^* + 3 jets with only LO accuracy, predicts a rate approximately 2–3 times smaller than the rate observed in data in this region.

Some $Z/\gamma^* +$jets observables have larger NLO-to-LO K-factors, defined as the ratio of the NLO prediction over the LO prediction, and are expected to have significant corrections at higher order than NLO [9]. The most remarkable example is the $H_{\mathrm{T}}^{\mathrm{jet}}$, defined as $H_{\mathrm{T}}^{\mathrm{jet}} = \sum p_{\mathrm{T}}^{\mathrm{jet}}$, in $Z/\gamma^* + \geqslant 1$ jet events. Figure 16 shows the measured cross section as a function of $H_{\mathrm{T}}^{\mathrm{jet}}$ compared to the available theoretical predictions. The NLO MCFM prediction fails to describe the shape of the $H_{\mathrm{T}}^{\mathrm{jet}}$ distribution, in particular it underestimates the measured cross section in the high $H_{\mathrm{T}}^{\mathrm{jet}}$ region, where the NLO-to-LO K-factor is greater than approximately two and a larger NLO scale-variation uncertainty is observed. The LO-ME+PS ALPGEN+PYTHIA prediction is in good agreement with data, but suffers for the large LO scale uncertainty. The POWHEG+PYTHIA prediction also is in good agreement with data, but is still affected by the larger NLO scale-variation uncertainty in the high p_{T} tail. The $\bar{\mathrm{n}}$NLO LOOPSIM+MCFM prediction provides a good modeling of the data distribution, and shows a significantly reduced scale-variation uncertainty.

C. Cross section for the production of a Z/γ^* boson in association with two or more jets

Figures 17 to 23 show measured differential cross sections in the $Z/\gamma^* + \geqslant 2$ jets final state. Figures 17 and 18 show the measured cross section as a function of the 2*nd* leading jet p_{T} and inclusive jet rapidity compared to ALPGEN+PYTHIA and BLACKHAT+SHERPA predictions. Measured distributions are in good agreement with the theoretical predictions. Figure 19 shows the measured cross section as a function of the dijet mass, M_{jj}. The cross section in the first bin is overes-

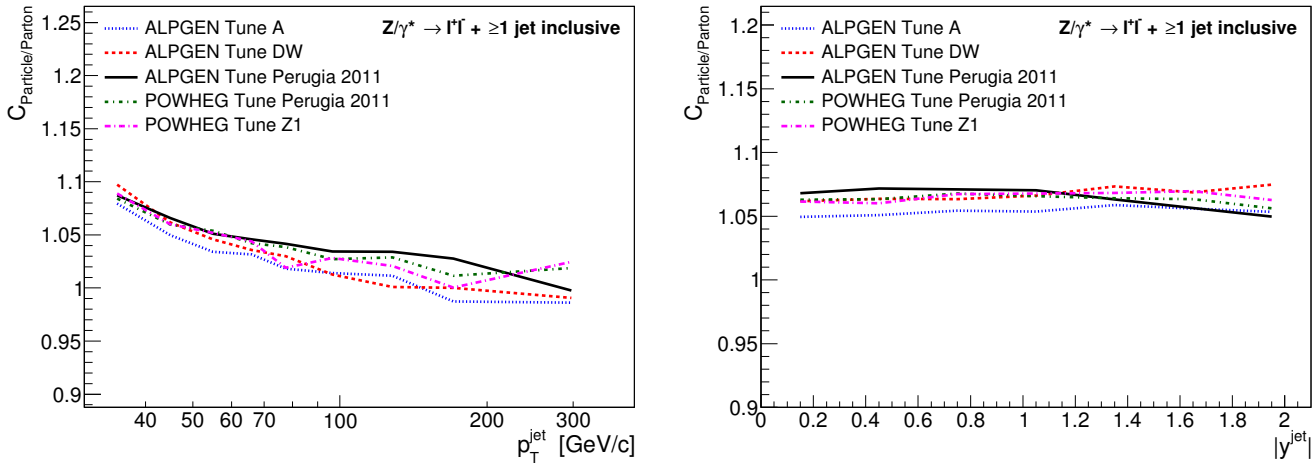

(a) (b)

FIG. 5. Parton-to-particle corrections as functions of (a) inclusive jet p_{T} and (b) inclusive jet rapidity for $Z/\gamma^* + \geqslant 1$ jet events, with various choices of the PYTHIA tune and different matrix element generators ALPGEN or POWHEG.

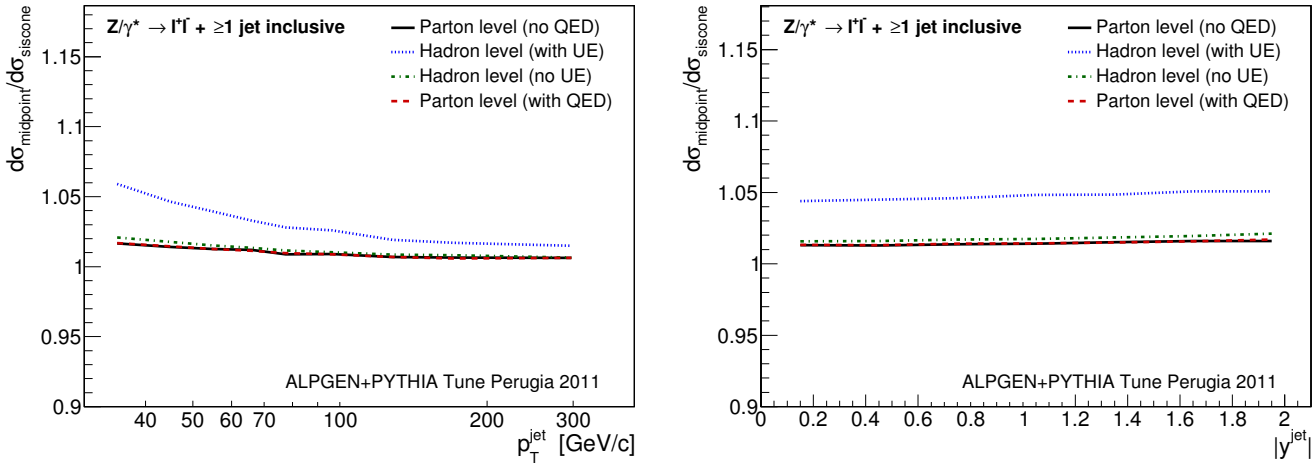

(a) (b)

FIG. 6. Ratio of differential cross sections evaluated with the midpoint and with the SISCone jet algorithms, as functions of (a) inclusive jet p_{T} and (b) inclusive jet rapidity in $Z/\gamma^* + \geqslant 1$ jet events.

timated by the MCFM prediction, but correctly described by the ALPGEN+PYTHIA prediction. In the M_{jj} region above approximately 160 GeV/c^2, the measured cross sections are $10\% - 20\%$ higher than both predictions. However, the systematic uncertainty, mainly due to the jet-energy scale, is as large as the observed difference. Figure 20 shows the measured cross section as a function of the dijet ΔR compared to ALPGEN+PYTHIA and MCFM predictions. Some differences between data and theory are observed at high ΔR, where the measured cross section is approximately 50% higher than the theoretical predictions. The dijet $\Delta\phi$ and Δy differential cross sections also are measured, and the results are shown in Figs. 21 and 22. The dijet $\Delta\phi$ appears reasonably modeled by the ALPGEN+PYTHIA and MCFM predictions, whereas the dijet Δy shows a shape difference, which reaches 50% at $\Delta y = 3 - 3.6$, and is related to the observed difference between data and theory at $\Delta R \gtrsim 4$. This region is affected by large experimental uncertainties, mainly due to the pile-up subtraction, and large theoretical uncertainty. Figure 23 shows the measured cross section as a function of the dihedral angle $\theta_{Z,jj}$ between the $Z/\gamma^* \to \ell^+\ell^-$ decay plane and the jet-jet plane [59]. The measured cross section is in good agreement with the ALPGEN+PYTHIA and MCFM predictions.

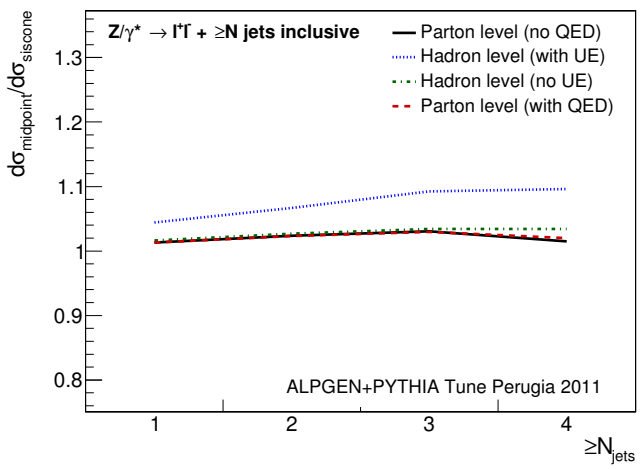

FIG. 7. Ratio of differential cross sections evaluated with the midpoint and with the SISCone jet algorithms, as a function of jet multiplicity in $Z/\gamma^* + \geqslant N_{\text{jets}}$.

D. Cross section for the production of a Z/γ^* boson in association with three or more jets

Figure 24 shows the differential cross sections as a functions of 3*rd* leading jet p_{T} and inclusive jet rapidity in events with a reconstructed $Z/\gamma^* \to \ell^+\ell^-$ decay and at least three jets. The NLO BLACKHAT+SHERPA prediction is approximately 30% lower than the measured cross sections for Z/γ^* + $\geqslant 3$ jets events, but data and predictions are still compatible within the approximately 25% scale-variation uncertainty and the 15% systematic uncertainty, dominated by the jet-energy scale. Apart from the difference in the normalization, the shape of the measured differential cross sections is in good agreement with the NLO BLACKHAT+SHERPA prediction.

X. SUMMARY AND CONCLUSIONS

The analysis of the full proton-antiproton collisions sample collected with the CDF II detector in Run II of the Tevatron, corresponding to 9.6 fb^{-1} integrated luminosity, allows for precise measurements of $Z/\gamma^* + \text{jets}$ inclusive and differential cross sections, which constitute an important legacy of the Tevatron physics program. The cross sections are measured using the decay channels $Z/\gamma^* \to e^+e^-$ and $Z/\gamma^* \to \mu^+\mu^-$ in the kinematic region $p_{\text{T}}^{\ell} \geqslant 25$ GeV/c, $|\eta^{\ell}| \leqslant 1$, $66 \leqslant M_{\ell^+\ell^-} \leqslant 116$ GeV/c^2, $p_{\text{T}}^{\text{jet}} \geqslant 30$ GeV/c, $|y^{\text{jet}}| \leqslant 2.1$, and $\Delta R_{\ell-\text{jet}} \geqslant 0.7$, with jets reconstructed using the midpoint algorithm in a radius $R = 0.7$. The measured cross sections are unfolded to the particle level and the decay channels combined. Results are compared with the most recent theoretical predictions, which properly model the measured differential cross sections in $Z/\gamma^* + \geqslant 1$, 2, and 3 jets final states. The main experimental uncertainty is related to the jet-energy scale, whereas the largest uncertainty of the theoretical predictions is generally associated with the variation of the renormalization and factorization scales. Among perturbative QCD predictions, LOOPSIM+MCFM shows the lowest scale-variation uncertainty and, therefore, gives the most accurate cross-section prediction for the $Z/\gamma^* + \geqslant 1$ jet final state. The MCFM and BLACKHAT+SHERPA fixed-order NLO predictions are in reasonable agreement with the data in the $Z/\gamma^* + \geqslant 1$, 2, and 3 jets final states. The ALPGEN+PYTHIA prediction provides a good modeling of differential distributions for all jets multiplicities. The POWHEG+PYTHIA prediction, due to the NLO accuracy of the matrix elements and to the inclusion of nonperturbative QCD effects, provides precise modeling of $Z/\gamma^* + \geqslant 1$ jet final states both in the low- and high-p_{T} kinematic regions. The effect of NLO electroweak virtual corrections to the Z/γ^* + jet production is studied and included in the comparison with the measured cross sections: in the high p_{T} kinematic region, corrections are of the order of 5%, which is comparable with the accuracy of predictions at higher order than NLO. The large theoretical uncertainty associated with the variation of the renormalization and factorization scales suggests that the inclusion of higher order QCD corrections, by mean of exact or approximate calculations, will improve the theoretical modeling of $Z/\gamma^* + \text{jets}$ processes.

The understanding of associated production of vector bosons and jets is fundamental in searches for non-SM physics, and the results presented in this paper support the modeling of $Z/\gamma^* + \text{jets}$ currently employed in Higgs-boson measurements and searches for physics beyond the standard model.

ACKNOWLEDGMENTS

We thank the Fermilab staff and the technical staffs of the participating institutions for their vital contributions. This work was supported by the U.S. Department of Energy and National Science Foundation; the Italian Istituto Nazionale di Fisica Nucleare; the Ministry of Education, Culture, Sports, Science and Technology of Japan; the Natural Sciences and Engineering Research Council of Canada; the National Science Council of the Republic of China; the Swiss National Science Foundation; the A.P. Sloan Foundation; the Bundesministerium für Bildung und Forschung, Germany; the Korean World Class University Program, the National Research Foundation of Korea; the Science and Technology Facilities Council and the Royal Society, UK; the Russian Foundation for Basic Research; the Ministerio de Ciencia e Innovación, and Programa Consolider-Ingenio 2010, Spain; the Slovak R&D Agency; the Academy of Finland; the Australian Research Council (ARC); and the EU community Marie Curie Fellowship contract 302103.

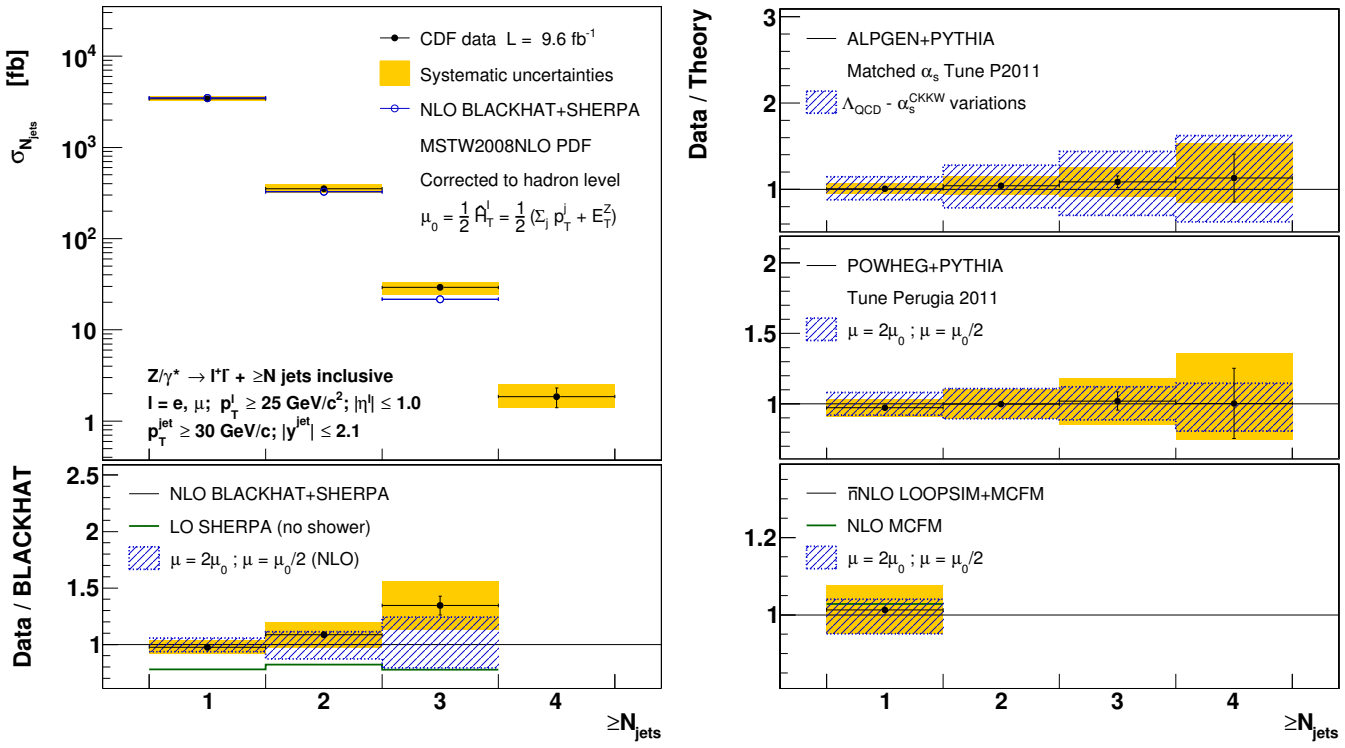

FIG. 8. Inclusive $Z/\gamma^* + \geqslant N$ jets cross section as a function of jet multiplicity. The measured cross section (black dots) is compared to the BLACKHAT+SHERPA NLO prediction (open circles). The black vertical bars show the statistical uncertainty, and the yellow bands show the total systematic uncertainty, except for the 5.8% uncertainty on the luminosity. The lower and right panels show the data-to-theory ratio with respect to other theoretical predictions, with the blue dashed bands showing the scale-variation uncertainty of each prediction, which is associated with the variation of the renormalization and factorization scales μ or to the combined variation of α_s^{CKKW} and Λ_{QCD}.

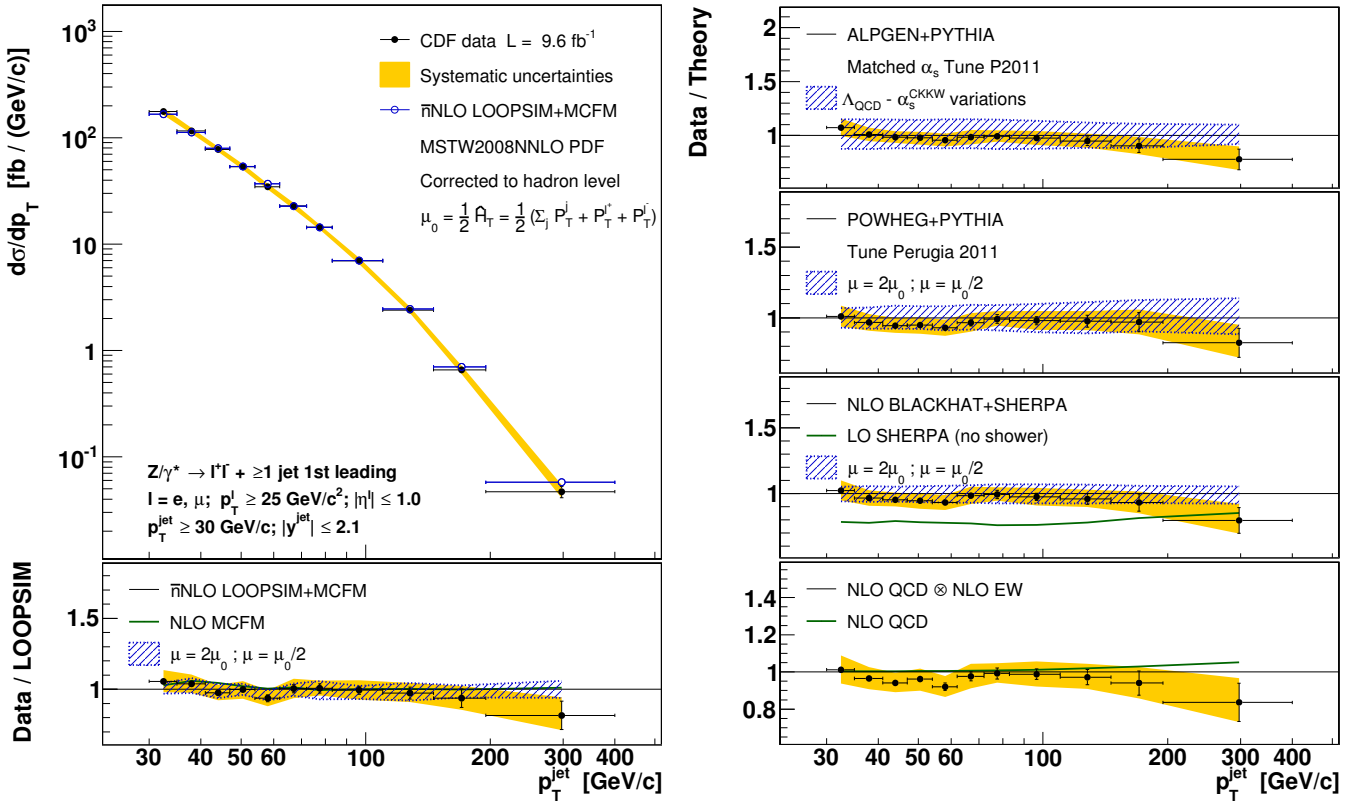

FIG. 9. Differential cross section as a function of leading jet p_{T} for $Z/\gamma^* + \geqslant 1$ jet events. The measured cross section (black dots) is compared to the LOOPSIM+MCFM $\bar{n}$NLO prediction (open circles). The black vertical bars show the statistical uncertainty, and the yellow bands show the total systematic uncertainty, except for the 5.8% uncertainty on the luminosity. The lower and right panels show the data-to-theory ratio with respect to other theoretical predictions, with the blue dashed bands showing the scale-variation uncertainty of each prediction, which is associated with the variation of the renormalization and factorization scales μ or to the combined variation of α_s^{CKKW} and Λ_{QCD}.

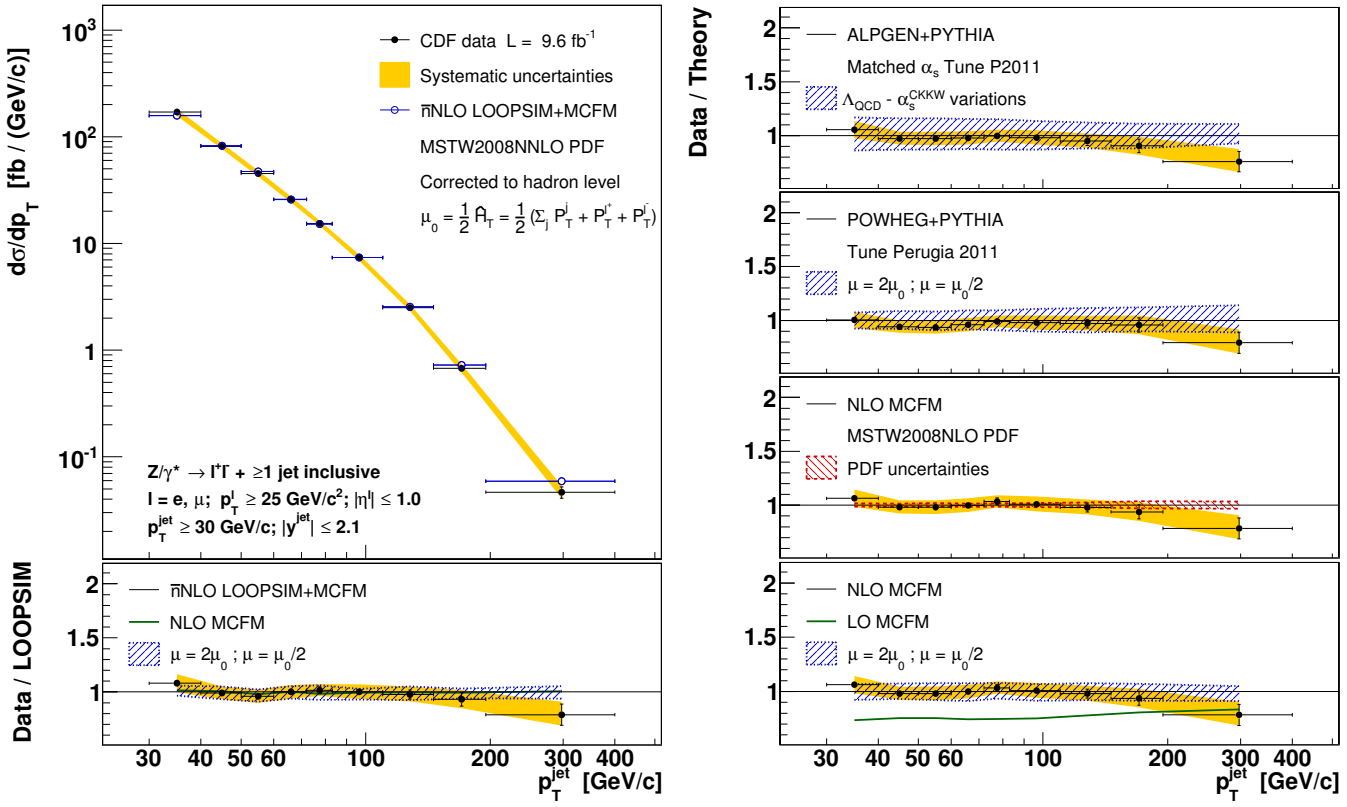

FIG. 10. Differential cross section as a function of inclusive jet p_{T} for $Z/\gamma^* + \geqslant 1$ jet events. The measured cross section (black dots) is compared to the LOOPSIM+MCFM $\bar{n}$NLO prediction (open circles). The black vertical bars show the statistical uncertainty, and the yellow bands show the total systematic uncertainty, except for the 5.8% uncertainty on the luminosity. The lower and right panels show the data-to-theory ratio with respect to other theoretical predictions with the blue dashed bands showing the scale-variation uncertainty of each prediction, which is associated with the variation of the renormalization and factorization scales μ or to the combined variation of α_s^{CKKW} and Λ_{QCD}. The red dashed band shows the PDF uncertainty evaluated with the MCFM prediction.

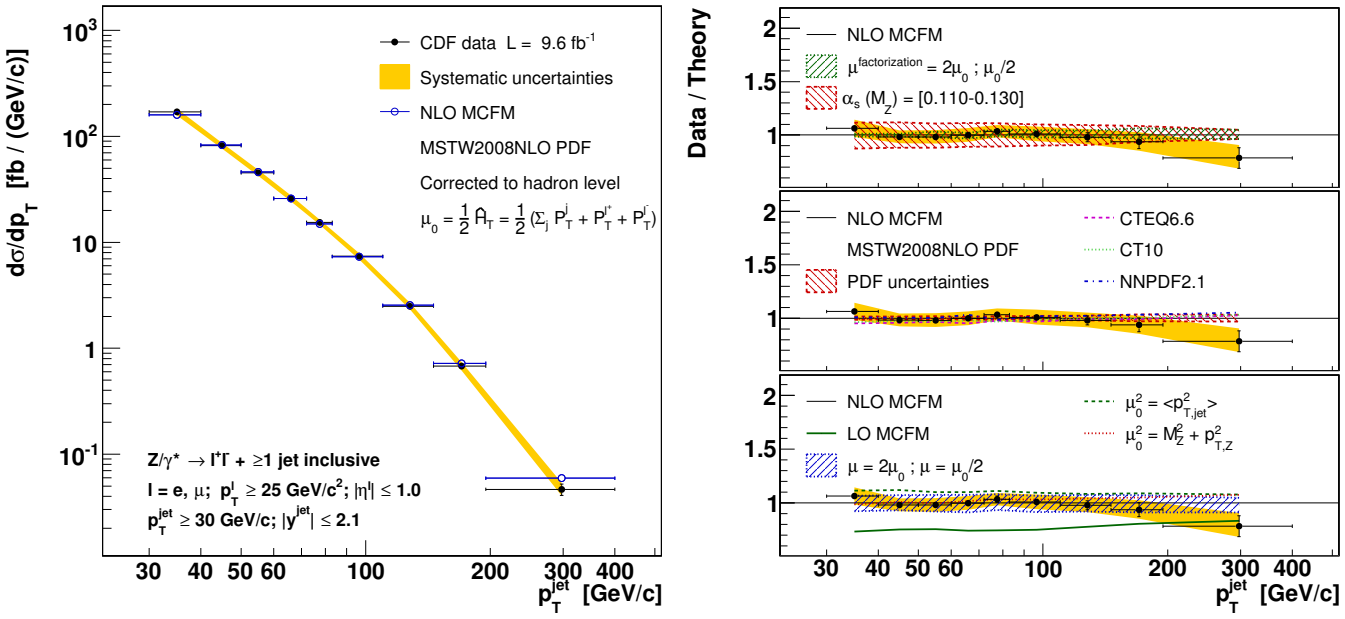

FIG. 11. Differential cross section as a function of inclusive jet p_{T} for $Z/\gamma^{*}+\geqslant 1$ jet events. The measured cross section (black dots) is compared to the MCFM NLO prediction (open circles). The black vertical bars show the statistical uncertainty, and the yellow bands show the total systematic uncertainty, except for the 5.8% uncertainty on the luminosity. The right panels show, from top to bottom, the data-to-theory ratio including variations of $\alpha_s(M_Z)$ (red dashed band) and factorization scale (green dashed band); various PDF sets and PDF uncertainty (red dashed band); and various choice of the functional form of the factorization and renormalization scales and scale-variation uncertainty (blue dashed band).

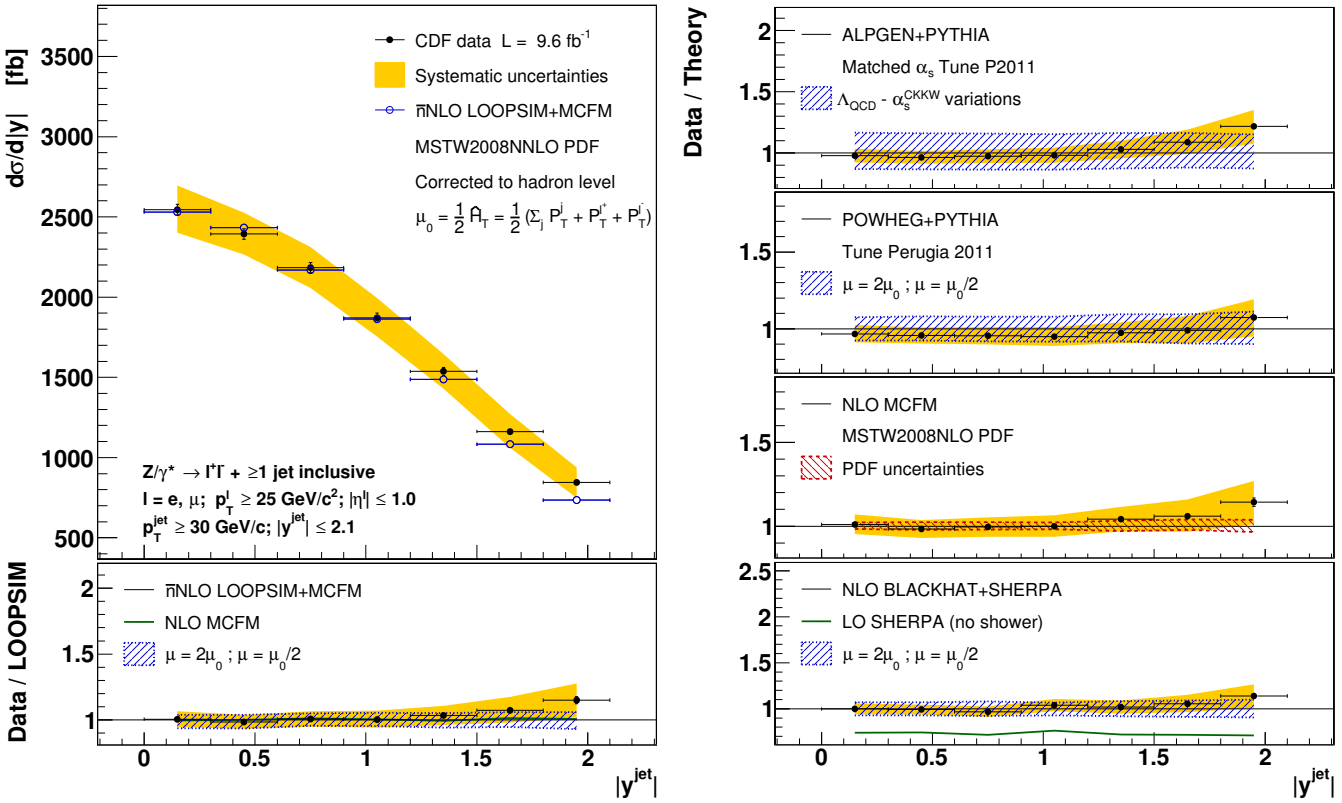

FIG. 12. Differential cross section as a function of inclusive jet rapidity for $Z/\gamma^* + \geqslant 1$ jet events. The measured cross section (black dots) is compared to the LOOPSIM+MCFM $\bar{n}$NLO prediction (open circles). The black vertical bars show the statistical uncertainty, and the yellow bands show the total systematic uncertainty, except for the 5.8% uncertainty on the luminosity. The lower and right panels show the data-to-theory ratio with respect to other theoretical predictions, with the blue dashed bands showing the scale-variation uncertainty of each prediction, which is associated with the variation of the renormalization and factorization scales μ or to the combined variation of α_s^{CKKW} and Λ_{QCD}. The red dashed band shows the PDF uncertainty evaluated with the MCFM prediction.

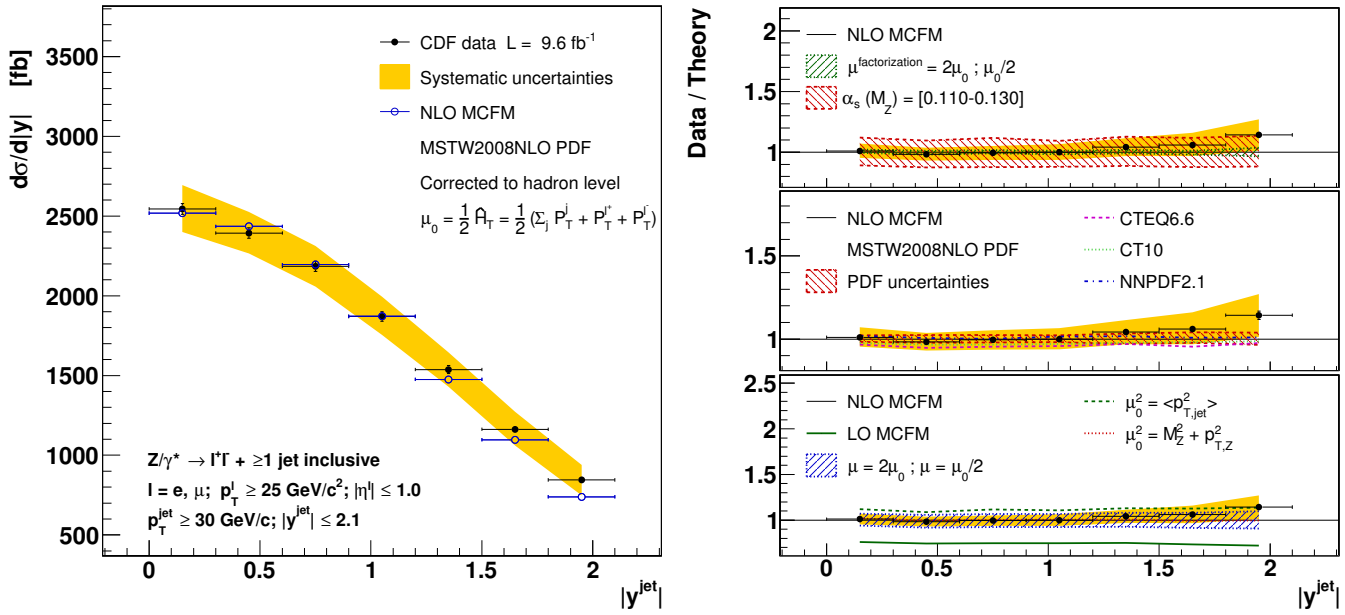

FIG. 13. Differential cross section as a function of inclusive jet rapidity for $Z/\gamma^* + \geqslant 1$ jet events. The measured cross section (black dots) is compared to the MCFM NLO prediction (open circles). The black vertical bars show the statistical uncertainty, and the yellow bands show the total systematic uncertainty, except for the 5.8% uncertainty on the luminosity. The right panels show, from top to bottom, the data-to-theory ratio including variations of $\alpha_s(M_Z)$ (red dashed band) and factorization scale (green dashed band); various PDF sets and PDF uncertainty (red dashed band); and various choice of the functional form of the factorization and renormalization scales and scale-variation uncertainty (blue dashed band).

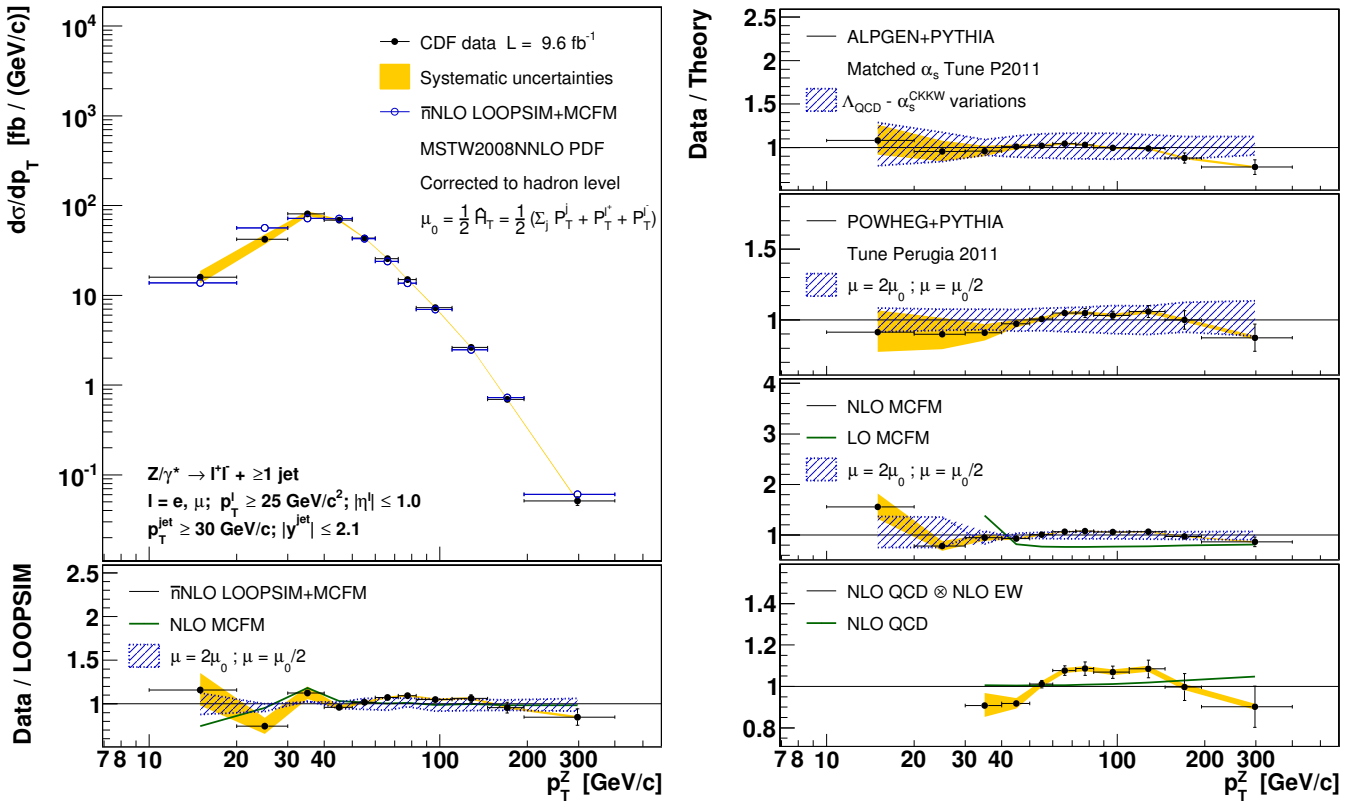

FIG. 14. Differential cross section as a function of Z/γ^* $p_{\rm T}$ for $Z/\gamma^* + \geqslant 1$ jet events. The measured cross section (black dots) is compared to the LOOPSIM+MCFM $\bar{n}$NLO prediction (open circles). The black vertical bars show the statistical uncertainty, and the yellow bands show the total systematic uncertainty, except for the 5.8% uncertainty on the luminosity. The lower and right panels show the data-to-theory ratio with respect to other theoretical predictions, with the blue dashed bands showing the scale-variation uncertainty of each prediction, which is associated with the variation of the renormalization and factorization scales μ or to the combined variation of $\alpha_s^{\rm CKKW}$ and Λ_{QCD}.

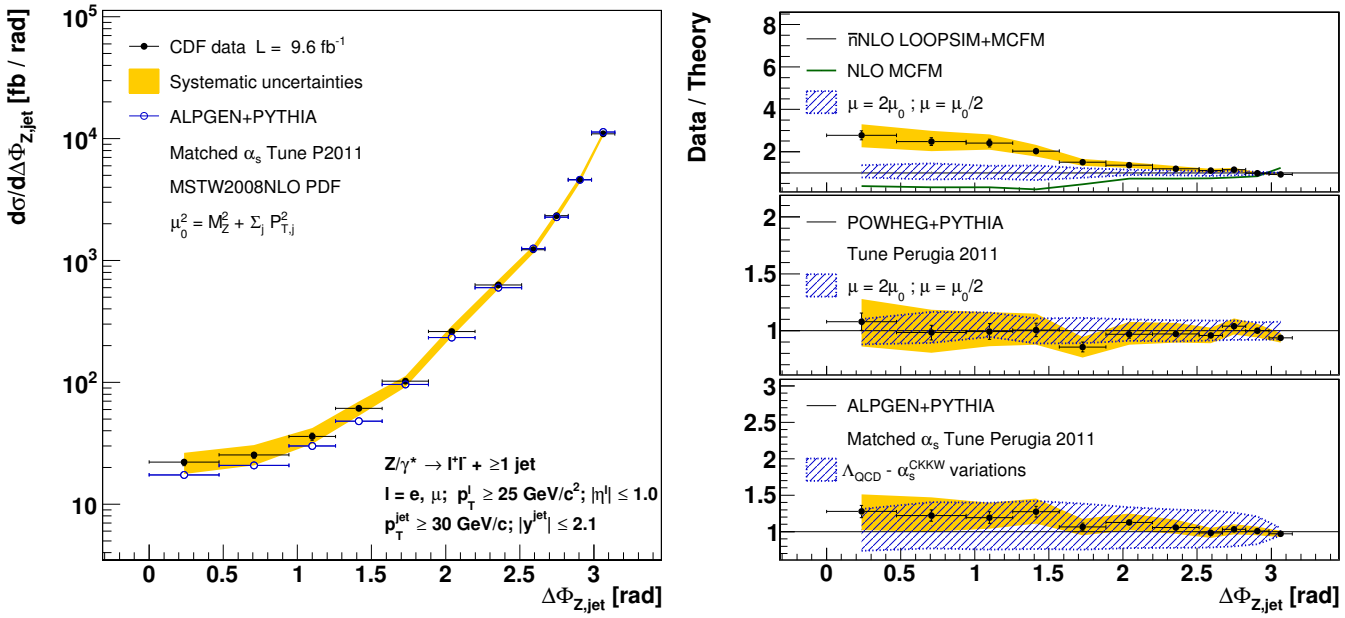

FIG. 15. Differential cross section as a function of Z/γ^*-jet $\Delta\phi$ for $Z/\gamma^* + \geqslant 1$ jet events. The measured cross section (black dots) is compared to the ALPGEN+PYTHIA prediction (open circles). The black vertical bars show the statistical uncertainty, and the yellow bands show the total systematic uncertainty, except for the 5.8% uncertainty on the luminosity. The right panels show the data-to-theory ratio with respect to other theoretical predictions, with the blue dashed bands showing the scale-variation uncertainty of each prediction, which is associated with the variation of the renormalization and factorization scales μ or to the combined variation of α_s^{CKKW} and Λ_{QCD}.

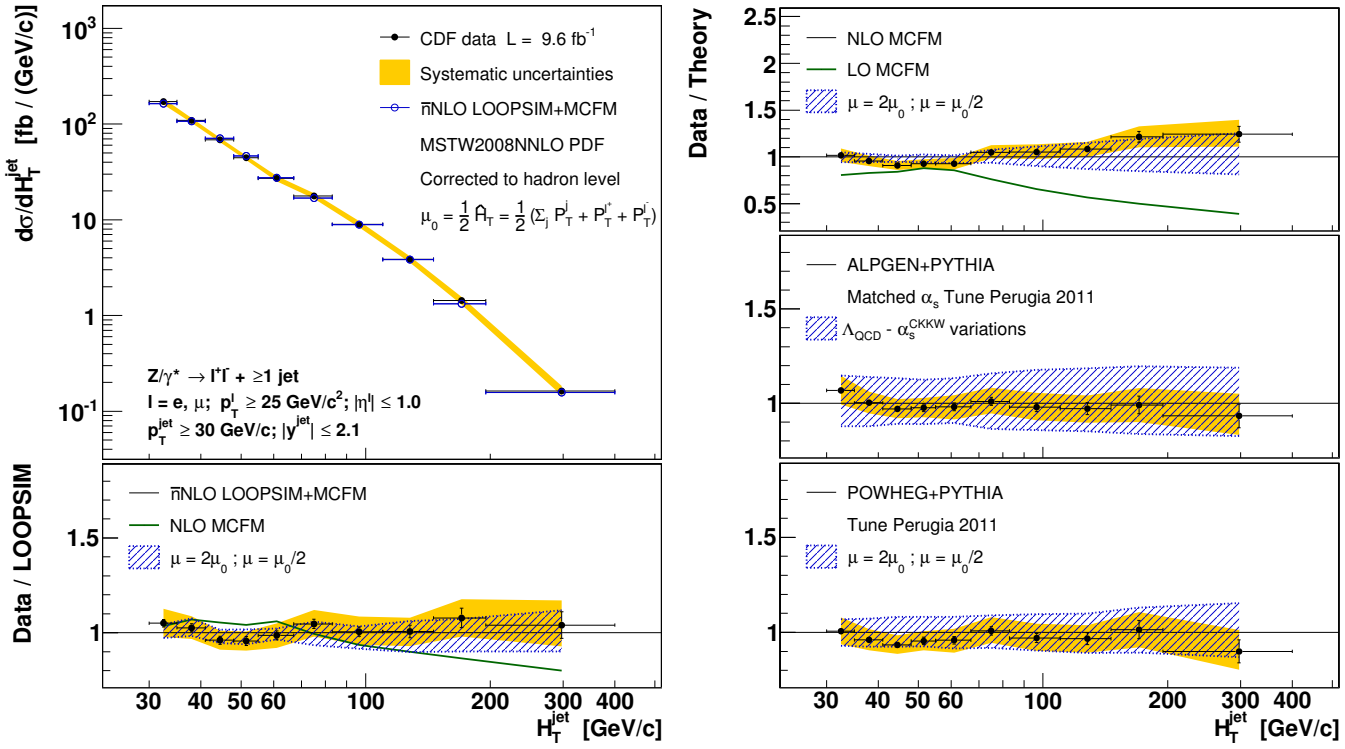

FIG. 16. Differential cross section as a function of $H_T^{\rm jet} = \sum p_T^{\rm jet}$ for $Z/\gamma^* + \geqslant 1$ jet events. The measured cross section (black dots) is compared to the LOOPSIM+MCFM $\bar{n}$NLO prediction (open circles). The black vertical bars show the statistical uncertainty, and the yellow bands show the total systematic uncertainty, except for the 5.8% uncertainty on the luminosity. The lower and right panels show the data-to-theory ratio with respect to other theoretical predictions, with the blue dashed bands showing the scale-variation uncertainty of each prediction, which is associated with the variation of the renormalization and factorization scales μ or to the combined variation of $\alpha_s^{\rm CKKW}$ and Λ_{QCD}.

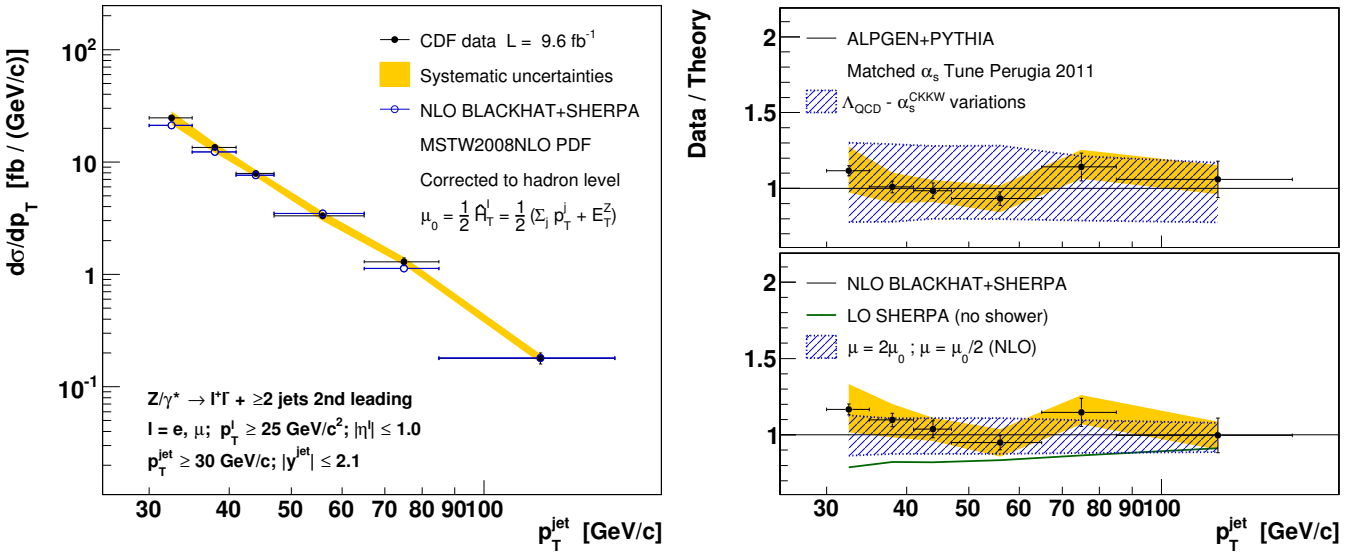

FIG. 17. Differential cross section as a function of 2*nd* leading jet p_T for $Z/\gamma^* + \geqslant 2$ jets events. The measured cross section (black dots) is compared to the BLACKHAT+SHERPA NLO prediction (open circles). The black vertical bars show the statistical uncertainty, and the yellow bands show the total systematic uncertainty, except for the 5.8% uncertainty on the luminosity. The right panels show the data-to-theory ratio with respect to ALPGEN+PYTHIA and BLACKHAT+SHERPA predictions, with the blue dashed bands showing the scale-variation uncertainty of each prediction, which is associated with the variation of the renormalization and factorization scales μ or to the combined variation of $\alpha_s^{\rm CKKW}$ and Λ_{QCD}.

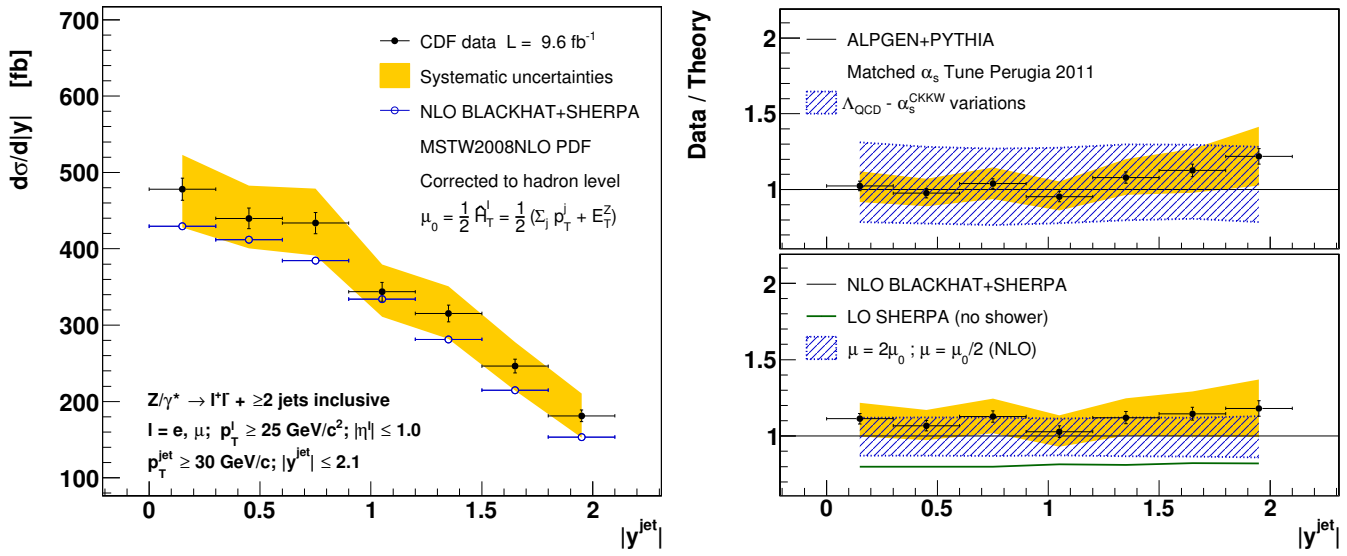

FIG. 18. Differential cross section as a function of inclusive jet rapidity for $Z/\gamma^* + \geqslant 2$ jets events. The measured cross section (black dots) is compared to the BLACKHAT+SHERPA NLO prediction (open circles). The black vertical bars show the statistical uncertainty, and the yellow bands show the total systematic uncertainty, except for the 5.8% uncertainty on the luminosity. The right panels show the data-to-theory ratio with respect to ALPGEN+PYTHIA and BLACKHAT+SHERPA predictions, with the blue dashed bands showing the scale-variation uncertainty of each prediction, which is associated with the variation of the renormalization and factorization scales μ or to the combined variation of α_s^{CKKW} and Λ_{QCD}.

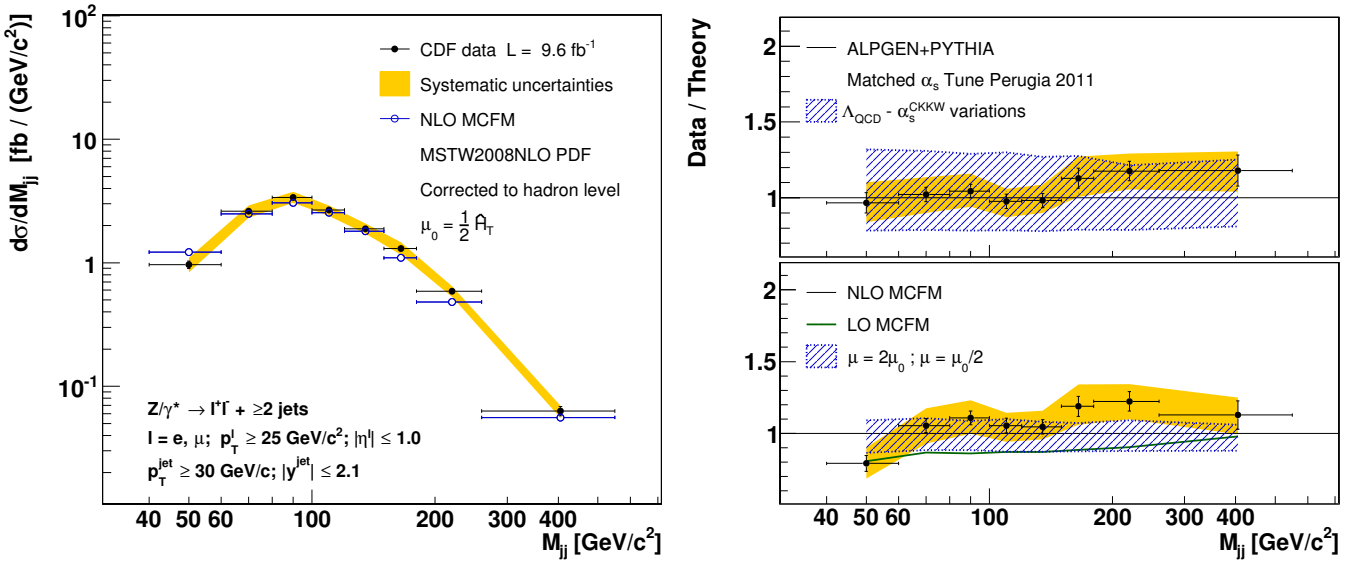

FIG. 19. Differential cross section as a function of dijet mass M_{jj} for $Z/\gamma^* + \geqslant 2$ jets events. The measured cross section (black dots) is compared to the MCFM NLO prediction (open circles). The black vertical bars show the statistical uncertainty, and the yellow bands show the total systematic uncertainty, except for the 5.8% uncertainty on the luminosity. The right panels show the data-to-theory ratio with respect to ALPGEN+PYTHIA and MCFM predictions, with the blue dashed bands showing the scale-variation uncertainty of each prediction, which is associated with the variation of the renormalization and factorization scales μ or to the combined variation of α_s^{CKKW} and Λ_{QCD}.

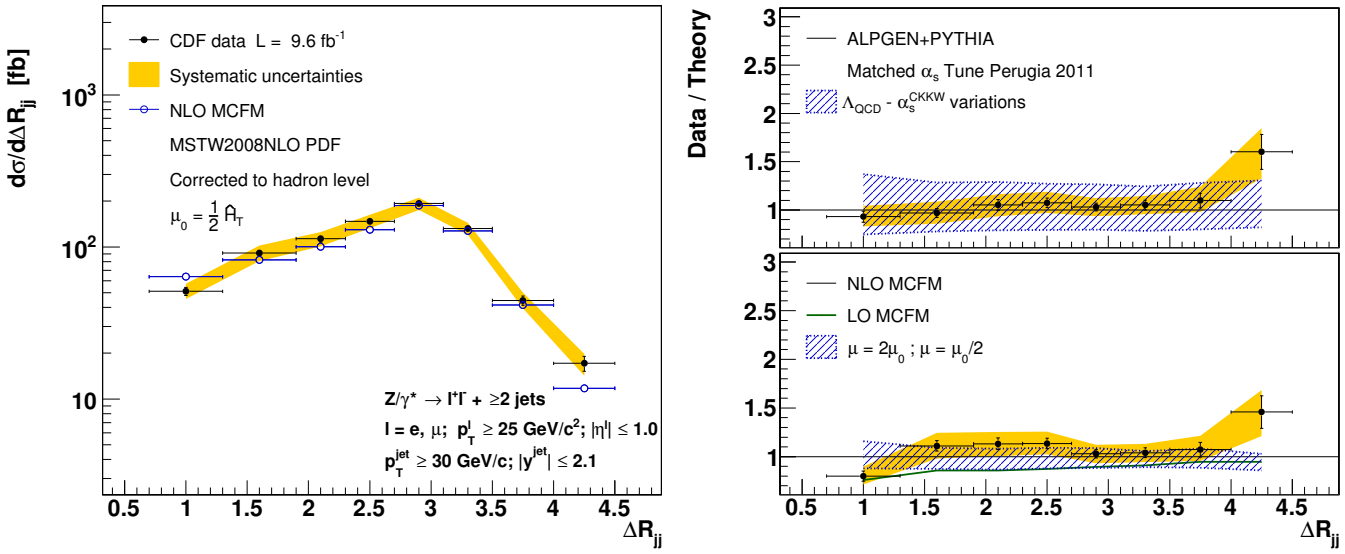

FIG. 20. Differential cross section as a function of dijet ΔR for $Z/\gamma^* + \geq 2$ jets events. The measured cross section (black dots) is compared to the MCFM NLO prediction (open circles). The black vertical bars show the statistical uncertainty, and the yellow bands show the total systematic uncertainty, except for the 5.8% uncertainty on the luminosity. The right panels show the data-to-theory ratio with respect to ALPGEN+PYTHIA and MCFM predictions, with the blue dashed bands showing the scale-variation uncertainty of each prediction, which is associated with the variation of the renormalization and factorization scales μ or to the combined variation of α_s^{CKKW} and Λ_{QCD}.

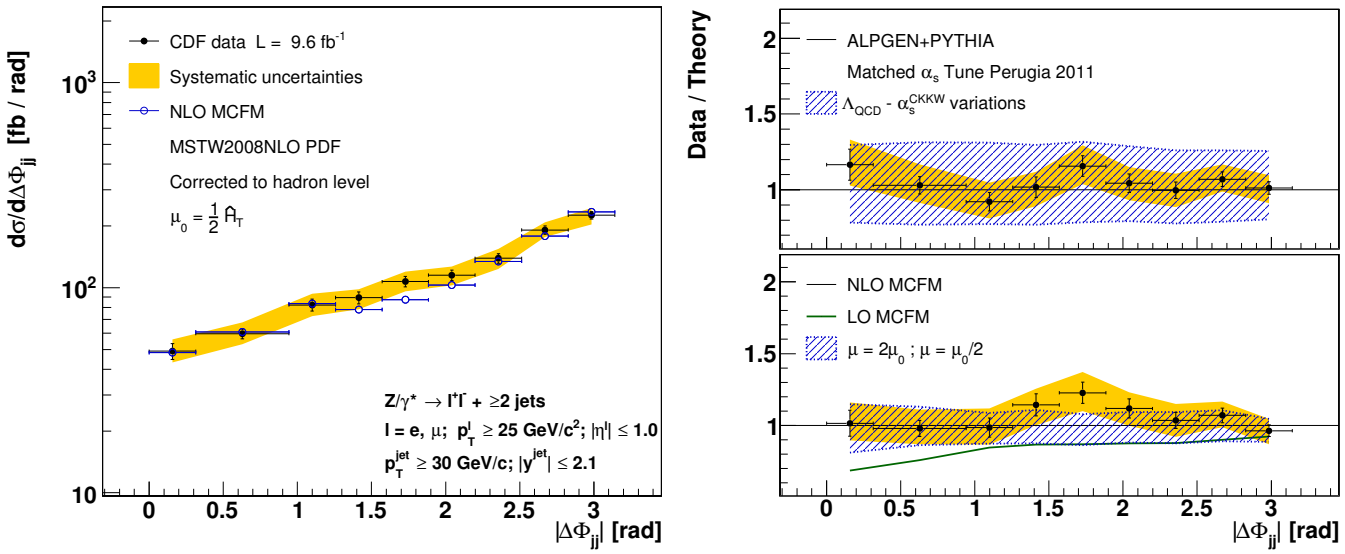

FIG. 21. Differential cross section as a function of dijet $\Delta\phi$ for $Z/\gamma^* + \geq 2$ jets events. The measured cross section (black dots) is compared to the MCFM NLO prediction (open circles). The black vertical bars show the statistical uncertainty, and the yellow bands show the total systematic uncertainty, except for the 5.8% uncertainty on the luminosity. The right panels show the data-to-theory ratio with respect to ALPGEN+PYTHIA and MCFM predictions, with the blue dashed bands showing the scale-variation uncertainty of each prediction, which is associated with the variation of the renormalization and factorization scales μ or to the combined variation of α_s^{CKKW} and Λ_{QCD}.

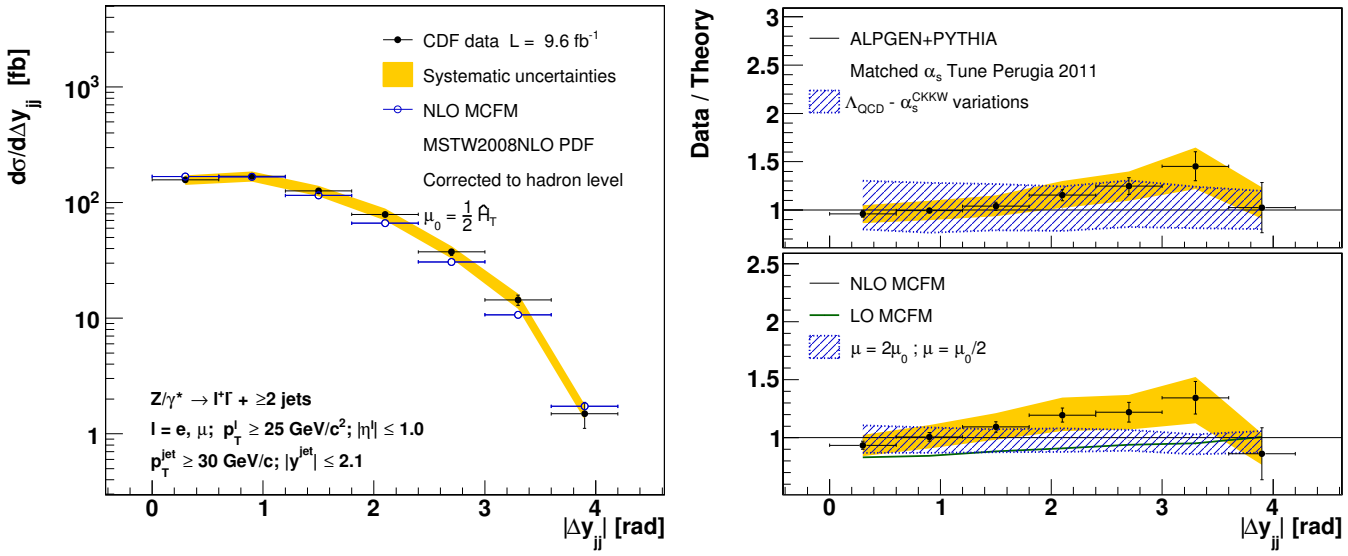

FIG. 22. Differential cross section as a function of dijet Δy for $Z/\gamma^* + \geqslant 2$ jets events. The measured cross section (black dots) is compared to the MCFM NLO prediction (open circles). The black vertical bars show the statistical uncertainty, and the yellow bands show the total systematic uncertainty, except for the 5.8% uncertainty on the luminosity. The right panels show the data-to-theory ratio with respect to ALPGEN+PYTHIA and MCFM predictions, with the blue dashed bands showing the scale-variation uncertainty of each prediction, which is associated with the variation of the renormalization and factorization scales μ or to the combined variation of α_s^{CKKW} and Λ_{QCD}.

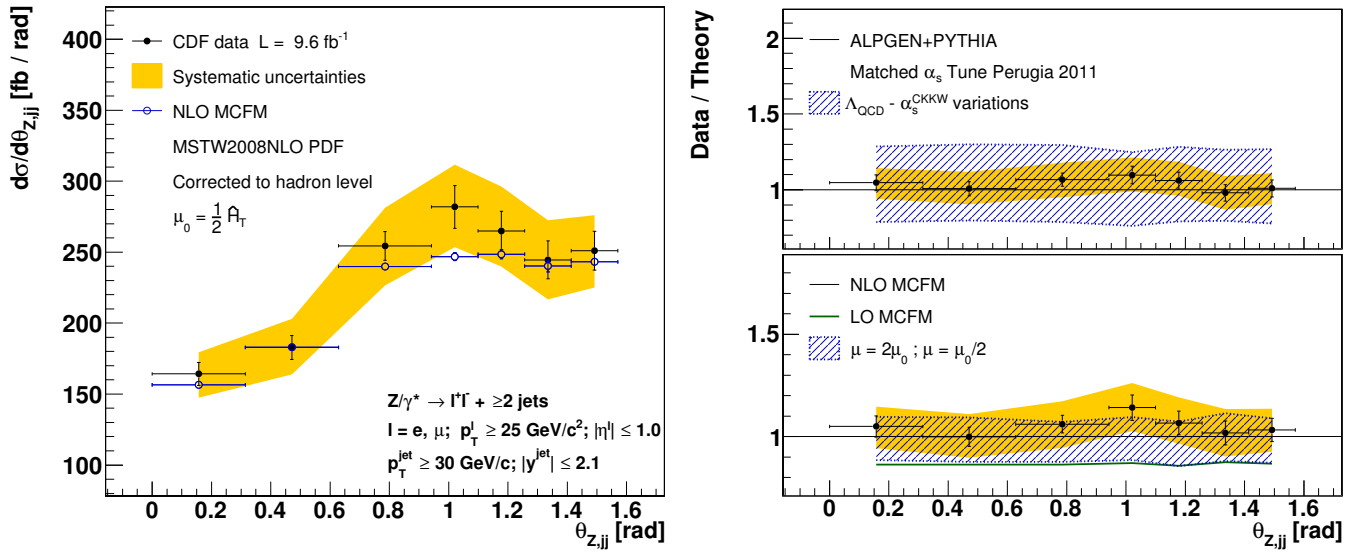

FIG. 23. Differential cross section as a function of the dihedral angle $\theta_{Z,jj}$ for $Z/\gamma^* + \geqslant 2$ jets events. The measured cross section (black dots) is compared to the MCFM NLO prediction (open circles). The black vertical bars show the statistical uncertainty, and the yellow bands show the total systematic uncertainty, except for the 5.8% uncertainty on the luminosity. The right panels show the data-to-theory ratio with respect to ALPGEN+PYTHIA and MCFM predictions, with the blue dashed bands showing the scale-variation uncertainty of each prediction, which is associated with the variation of the renormalization and factorization scales μ or to the combined variation of α_s^{CKKW} and Λ_{QCD}.

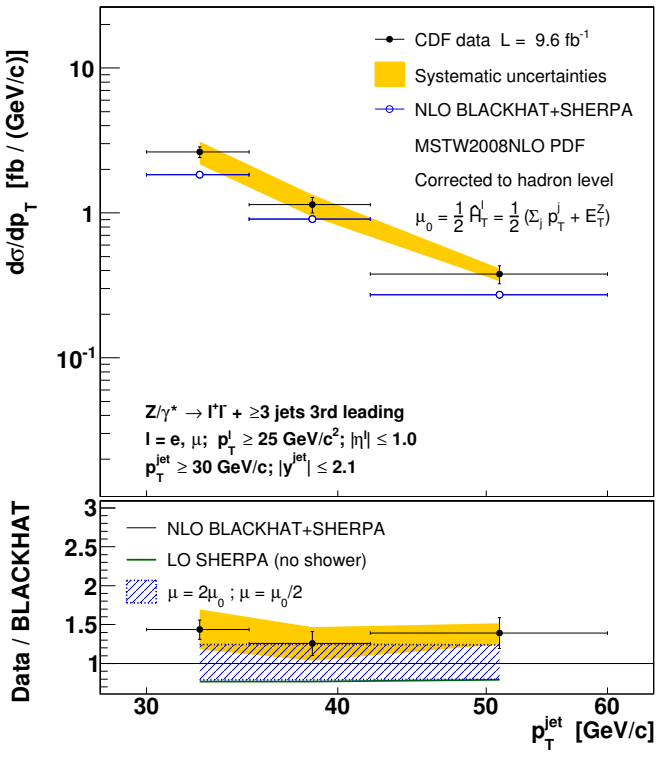

(a)

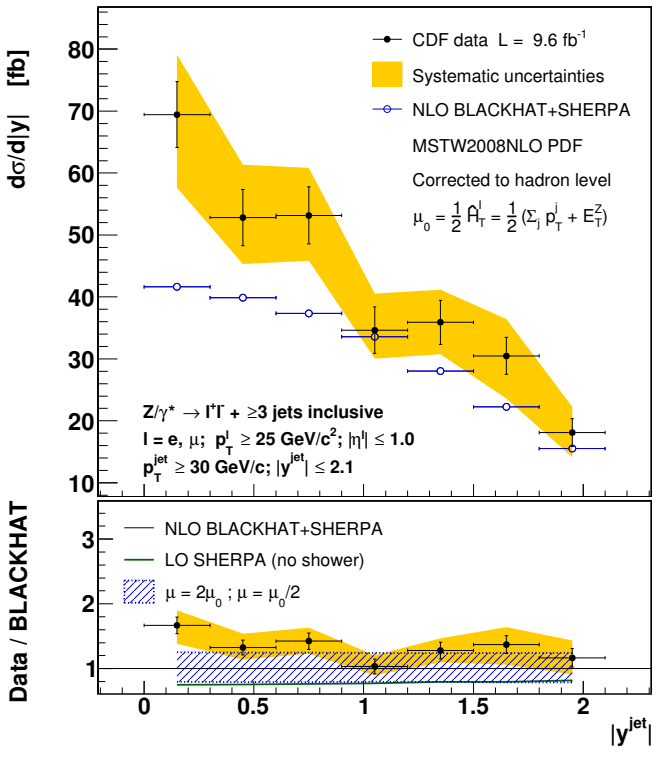

(b)

FIG. 24. Differential cross section as a function of (a) 3*rd* leading jet p_{T} and (b) inclusive jet rapidity for $Z/\gamma^{*}+\geqslant 3$ jets events. The measured cross section (black dots) is compared to the BLACKHAT+SHERPA NLO prediction (open circles). The black vertical bars show the statistical uncertainty, and the yellow bands show the total systematic uncertainty, except for the 5.8% uncertainty on the luminosity. The lower panels show the data-to-theory ratio, with the blue dashed bands showing the scale-variation uncertainty, which is associated with the variation of the renormalization and factorization scales μ.

[1] D. Gross and F. Wilczek, Phys. Rev. D **8**, 3633 (1973).
[2] T. Aaltonen *et al.* (CDF Collaboration), Phys. Rev. Lett. **100**, 102001 (2008).
[3] V. Abazov *et al.* (D0 Collaboration), Phys. Lett. B **669**, 278 (2008); Phys. Lett. B **678**, 45 (2009); Phys. Lett. B **682**, 370 (2010).
[4] G. Aad *et al.* (ATLAS Collaboration), J. High Energy Phys. 07 (2013) 032; Phys. Rev. D **85**, 032009 (2012).
[5] S. Chatrchyan *et al.* (CMS Collaboration), J. High Energy Phys. 01 (2012) 010; Phys. Lett. B **722**, 238 (2013); V. Khachatryan *et al.* (CMS Collaboration), (2014), arXiv:1408.3104 [hep-ex].
[6] The rapidity is defined as $y = \frac{1}{2}\ln(\frac{E+p_Z}{E-p_Z})$; the transverse momentum and energy are defined by $p_{\mathrm{T}} = p\sin\theta$ and $E_{\mathrm{T}} = E\sin\theta$.
[7] J. M. Campbell and R. K. Ellis, Phys. Rev. D **65**, 113007 (2002).
[8] C. Berger, Z. Bern, L. Dixon, F. Febres Cordero, D. Forde, H. Ita, D. A. Kosower, and D. Maitre, Phys. Rev. D **78**, 036003 (2008).
[9] M. Rubin, G. P. Salam, and S. Sapeta, J. High Energy Phys. 09 (2010) 084.
[10] A. Denner, S. Dittmaier, T. Kasprzik, and A. Mück, J. High Energy Phys. 06 (2011) 069.
[11] M. L. Mangano, M. Moretti, F. Piccinini, R. Pittau, and A. D. Polosa, J. High Energy Phys. 07 (2003) 001.
[12] S. Alioli, P. Nason, C. Oleari, and E. Re, J. High Energy Phys. 01 (2011) 095.
[13] A. Abulencia *et al.* (CDF Collaboration), J. Phys. G **34**, 2457 (2007).
[14] A. Sill (CDF Collaboration), Nucl. Instrum. Methods A **447**, 1 (2000).
[15] A. A. Affolder *et al.*, Nucl. Instrum. Methods A **526**, 249 (2004).
[16] L. Balka *et al.*, Nucl. Instrum. Methods A **267**, 272 (1988).
[17] S. Hahn *et al.*, Nucl. Instrum. Methods A **267**, 351 (1988).
[18] S. Bertolucci *et al.*, Nucl. Instrum. Methods A **267**, 301 (1988).
[19] G. Ascoli, L. Holloway, I. Karliner, U. Kruse, R. Sard, V. Simaitis, D. Smith, and T. Westhusing, Nucl. Instrum. Methods A **268**, 33 (1988).
[20] J. Elias, S. Klimenko, J. Konigsberg, A. Korytov, G. Mitselmakher, A. Nomerotski, D. Northacker, A. Safonov, and R. Vidal, Nucl. Instrum. Methods A **441**, 366 (2000).
[21] B. Winer, Int. J. Mod. Phys. **A16S1C**, 1169 (2001).
[22] A. Abulencia *et al.* (CDF Collaboration), Phys. Rev. D **74**, 071103 (2006).
[23] The jet cone radius R is defined as $R = \sqrt{\eta^2+\phi^2}$.
[24] The transverse energy is evaluated using the position of the tower with respect to the primary interaction vertex.
[25] G. C. Blazey *et al.*, FERMILAB-CONF-00-092-E (2000).
[26] A. Bhatti *et al.*, Nucl. Instrum. Methods A **566**, 375 (2006).
[27] ΔR is defined as $\Delta R = \sqrt{\Delta y^2+\Delta\phi^2}$.
[28] T. Sjöstrand, S. Mrenna, and P. Z. Skands, J. High Energy Phys. 05 (2006) 026.
[29] H. Lai, J. Huston, S. Kuhlmann, J. Morfin, F. Olness, J. Owens, J. Pumplin, and W. Tung, Eur. Phys. J. C **12**, 375 (2000).
[30] P. Z. Skands, Phys. Rev. D **82**, 074018 (2010).
[31] J. Alwall *et al.*, Eur. Phys. J. C **53**, 473 (2008).
[32] T. Affolder *et al.* (CDF Collaboration), Phys. Rev. D **65**, 092002 (2002).
[33] R. Brun, F. Bruyant, M. Maire, A. McPherson, and P. Zanarini, CERN-DD-EE-84-1 (1987).
[34] G. Grindhammer, M. Rudowicz, and S. Peters, Nucl. Instrum. Methods A **290**, 469 (1990).
[35] S. Moch and P. Uwer, Nucl. Phys. Proc. Suppl. **183**, 75 (2008).
[36] J. M. Campbell and R. K. Ellis, Phys. Rev. D **60**, 113006 (1999).
[37] C. Buttar *et al.*, (2008), arXiv:0803.0678 [hep-ph].
[38] S. Klimenko, J. Konigsberg, and T. M. Liss, FERMILAB-FN-0741 (2003).
[39] A. Martin, W. Stirling, R. Thorne, and G. Watt, Eur. Phys. J. C **63**, 189 (2009).
[40] J. Pumplin, D. Stump, R. Brock, D. Casey, J. Huston, J. Kalk, H. L. Lai, and W. K. Tung, Phys. Rev. D **65**, 014013 (2001).
[41] P. M. Nadolsky, H.-L. Lai, Q.-H. Cao, J. Huston, J. Pumplin, D. Stump, W.-K. Tung, and C.-P. Yuan, Phys. Rev. D **78**, 013004 (2008).
[42] R. D. Ball, V. Bertone, F. Cerutti, L. Del Debbio, S. Forte, A. Guffanti, J. I. Latorre, J. Rojo, and M. Ubiali (NNPDF Collaboration), Nucl. Phys. **B849**, 296 (2011).
[43] H.-L. Lai, M. Guzzi, J. Huston, Z. Li, P. M. Nadolsky, J. Pumplin, and C.-P. Yuan, Phys. Rev. D **82**, 074024 (2010).
[44] A. D. Martin, R. Roberts, W. Stirling, and R. Thorne, Eur. Phys. J. C **23**, 73 (2002).
[45] M. Whalley, D. Bourilkov, and R. Group, (2005), arXiv:hep-ph/0508110 [hep-ph].
[46] C. F. Berger, Z. Bern, L. J. Dixon, F. Febres Cordero, D. Forde, T. Gleisberg, H. Ita, D. A. Kosower, and D. Maître, Phys. Rev. D **82**, 074002 (2010); Phys. Rev. D **80**, 074036 (2009).
[47] C. W. Bauer and B. O. Lange, (2009), arXiv:0905.4739 [hep-ph].
[48] In BLACKHAT and POWHEG predictions, the alternative definition $\mu_0 = \hat{H'}_{\mathrm{T}}/2 = \frac{1}{2}\left(\sum_j p_{\mathrm{T}}^j + E_{\mathrm{T}}^Z\right)$ with $E_{\mathrm{T}}^Z = \sqrt{M_Z^2 + p_{\mathrm{T},Z}^2}$ is used, where the index j runs over the partons in the final state.
[49] S. Camarda, Ph.D. thesis, Universitat Autonoma de Barcelona, FERMILAB-THESIS-2012-12, 2012.
[50] S. Catani, F. Krauss, R. Kuhn, and B. Webber, J. High Energy Phys. 11 (2001) 063.
[51] B. Cooper, J. Katzy, M. Mangano, A. Messina, L. Mijovi, and P. Skands, Eur. Phys. J. C **72**, 2078 (2012).
[52] M. G. Albrow *et al.*, (2006), arXiv:hep-ph/0610012 [hep-ph]; R. Field, FERMILAB-PUB-06-408-E (2006).
[53] S. D. Ellis, Z. Kunszt, and D. E. Soper, Phys. Rev. Lett. **69**, 3615 (1992).
[54] M. Cacciari, G. P. Salam, and G. Soyez, Eur. Phys. J. C **72**, 1896 (2012).
[55] G. P. Salam and G. Soyez, J. High Energy Phys. 05 (2007) 086.
[56] R. Field, Acta Phys. Pol. B **42**, 2631 (2011).
[57] G. P. Salam, Eur. Phys. J. C **67**, 637 (2010).
[58] L. Lyons, D. Gibaut, and P. Clifford, Nucl. Instrum. Methods A **270**, 110 (1988).
[59] $\theta_{Z,jj}$ is defined as $\theta_{Z,jj} = \arccos\frac{(\vec{\ell}_1\times\vec{\ell}_2)\cdot(\vec{j}_1\times\vec{j}_2)}{|\vec{\ell}_1\times\vec{\ell}_2||\vec{j}_1\times\vec{j}_2|}$, where $\vec{\ell}$ and $\vec{j}$ are the momentum three-vectors of leptons and jets.